The Molecular and Electronic Structure of Isolated Platinum Sites Enabled by Expedient Measurement of ¹⁹⁵Pt Chemical Shift Anisotropy

Amrit Venkatesh,^{1,2} Domenico Gioffrè,³ Benjamin A. Atterberry,^{1,2} Lukas Rochlitz,³ Scott L. Carnahan,^{1,2} Zhuoran Wang,⁴ Georges Menzildjian,⁴ Anne Lesage,⁴* Christophe Copéret,³* Aaron J. Rossini^{1,2}*

¹Iowa State University, Department of Chemistry, Ames, IA, USA, 50011

²US DOE Ames Laboratory, Ames, Iowa, USA, 50011

³Department of Chemistry and Applied Biosciences, ETH Zürich, CH-8093 Zürich, Switzerland.

⁴Univ Lyon, ENS Lyon, Université Lyon 1, CNRS, High-Field NMR Center of Lyon, UMR 5082, F-69100 VILLEURBANNE, France.

Corresponding Authors

*e-mail: anne.lesage@ens-lyon.fr

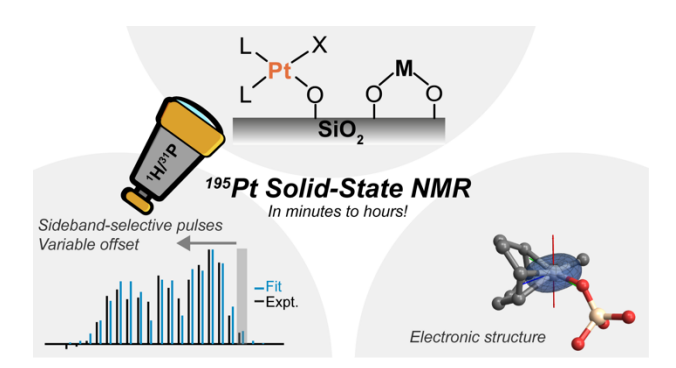
*e-mail: ccoperet@ethz.ch

*e-mail: arossini@iastate.edu

Abstract

Techniques that can characterize the molecular structures of dilute surface species are required to facilitate the rational synthesis and improvement of Pt-based heterogeneous catalysts. ¹⁹⁵Pt solid-state NMR spectroscopy could be an ideal tool for this task because ¹⁹⁵Pt isotropic chemical shifts and chemical shift anisotropy (CSA) are highly sensitive probes of the local chemical environment and electronic structure. However, characterization of Pt surface-sites is complicated by the typical low Pt loadings that are between 0.2 to 5 wt.% and broadening of ¹⁹⁵Pt solid-state NMR spectra by CSA. Here, we introduce a set of solid-state NMR methods that exploit fast MAS and indirect detection using a sensitive spy nucleus (¹H or ³¹P) to enable rapid acquisition of ¹⁹⁵Pt MAS NMR spectra. We demonstrate that high-resolution wideline ¹⁹⁵Pt MAS NMR spectra can be acquired in minutes to a few hours for a series of molecular and single-site Pt species grafted on silica with Pt loading of only 3-5 wt.%. Low-power, long-duration, sideband-selective excitation and saturation pulses are incorporated into t_1 -noise eliminated (TONE) dipolar heteronuclear multiple quantum coherence (D-HMQC), perfect echo resonance echo saturation pulse double resonance (PE RESPDOR) or *J*-resolved pulse sequences. The complete ¹⁹⁵Pt MAS NMR spectrum is then reconstructed by recording a series of 1D NMR spectra where the offset of the ¹⁹⁵Pt pulses is varied. Analysis of the ¹⁹⁵Pt MAS NMR spectra yields the ¹⁹⁵Pt chemical shift tensor parameters. Zeroth order approximation (ZORA) DFT calculations accurately predict ¹⁹⁵Pt CS tensor parameters. Simple and predictive orbital models relate the CS tensor parameters to the Pt electronic structure and coordination environment. The methodology developed here paves the way for the detailed structural and electronic analysis of dilute platinum surface-sites.

TOC Graphic



Introduction

Heterogeneous catalysis is widely used in industrial chemistry and is vital to sustainable chemical processes. 1-5 Recently, single-site 6-7 and single-atom a catalysts have emerged as a distinct class of highly efficient heterogeneous catalysts that display unique reactivity, increased catalytic efficiency and improved precious metal utilization. The ultimate goal in catalysis science is to derive detailed structure-activity relationship for rational development. The search for single-site catalysts that comprise of a well-defined coordination environment has thus been an active field of research. In this context, Surface Organometallic Chemistry (SOMC) has emerged as a powerful approach that relies on the controlled reaction of tailored molecular precursors with the functionality of supports, such as the isolated OH groups of oxide materials. 9-11 These well-defined surface species can be used directly as single-site catalysts or as precursors to i) generate isolated metal sites with defined oxidation state and nuclearity, or ii) control the interface, growth and composition of supported nanoparticles. 12-16 A key aspect of SOMC is the need to obtain an atomic-level characterization of surface species, using in particular solid-state nuclear magnetic resonance (NMR) spectroscopy. 5, 17-23

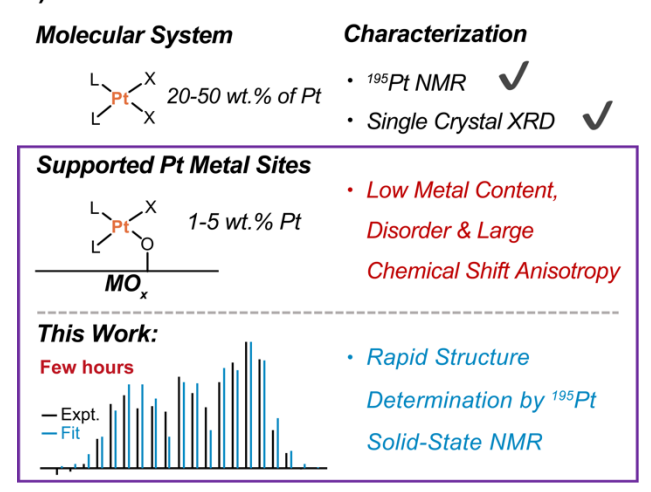
Solid-state NMR spectroscopy has been used to determine the three-dimensional structure of surface single-sites with a sub-angstrom precision.²⁴⁻²⁵ The complete measurement of the NMR chemical shift tensor via determination of the isotropic chemical shift and the chemical shift anisotropy (CSA) provides a fingerprint of the electronic structure and symmetry of an atomic environment.²⁶⁻²⁹ For example, differences in magnitude of the CSA (the span), determined experimentally, and the computed orientation of the chemical shift tensors can be traced back to specific molecular frontier orbitals and their relative energies in organometallic complexes; this has been used for instance to predict the reactivity of alkene and alkyne metathesis catalysts,³⁰⁻³⁴

unravel the electronic structure of organo-tellurides³⁵ and understand the π-accepting abilities of carbenes.³⁶⁻³⁸ Many metal-based catalysts have spin-1/2 isotopes which can be directly probed by solid-state NMR spectroscopy (⁸⁹Y, ¹⁰³Rh, ¹⁰⁹Ag, ¹¹³Cd, ¹¹⁹Sn, ¹⁸³W, ¹⁹⁹Hg, ¹⁹⁵Pt, ²⁰⁷Pb, etc.). However, direct NMR experiments on the metal nucleus of supported catalysts are challenging because of the typically low metal loadings. Consequently, NMR experiments have traditionally been limited to highly receptive isotopes of metals such as aluminum,³⁹ scandium,²¹ vanadium,⁴⁰⁻⁴¹ niobium¹⁸ and/or isotopically enriched materials.^{22, 42-43} Recently, sensitivity-enhancement by dynamic nuclear polarization (DNP) or proton detection has enabled NMR experiments on catalysts featuring unreceptive nuclei.⁴⁴⁻⁴⁹

The noble metal platinum is utilized in numerous catalytic processes.^{8,50-52} However, Pt(II) sites typically adopt a square-planar geometry, giving rise to very large ¹⁹⁵Pt CSA, reaching several thousand ppm and making acquisition of ¹⁹⁵Pt solid-state NMR spectra challenging.⁵³⁻⁵⁵ Yet, measurement of ¹⁹⁵Pt isotropic chemical shifts and CSA provides invaluable information by providing direct insight into the identity and symmetry of atoms within the Pt coordination sphere as well as a full understanding of its electronic structure.⁵⁵⁻⁶⁰ Towards this goal, various schemes have been proposed for the acquisition of wideline solid-state NMR spectra.^{53,61-63} DNP has been used to enhance further the sensitivity of wideline solid-state NMR experiments under static^{46,64-65} and moderate magic angle spinning (MAS) conditions.⁴⁹ However, these methods offer poor ¹⁹⁵Pt NMR resolution. Recently, we used static DNP experiments to characterize a model Pt single-site catalyst at 3.7 wt.% Pt loading, however even with DNP, six days of acquisition time was required to measure the ¹⁹⁵Pt CSA.⁶⁶ A rapidly developing approach to improve the sensitivity and resolution of solid-state NMR experiments, which can be readily applied with standard solid-state NMR spectrometers, is indirect detection of insensitive nuclei under fast MAS.⁶⁷⁻⁷⁰

In this work, we demonstrate that 195 Pt chemical shift tensors can be measured with high resolution in only minutes to hours for a series of molecular and single-site Pt species grafted on silica with Pt loading of only 3-5 wt.% (Figure 1). Our approach consists in the incorporation of long duration, low-power, sideband-selective pulses into indirect detection 1 H{ 195 Pt} t_{1} -noise eliminated heteronuclear multiple quantum coherence (TONE D-HMQC), perfect echo resonance echo saturation pulse double resonance (PE RESPDOR) and 31 P{ 195 Pt} J-resolved or J-HMQC pulse sequences all of which are performed with fast MAS ($v_{rot} \ge 25$ kHz). By varying the offset of the sideband-selective pulses across the 195 Pt spectrum and monitoring the 1D NMR signal intensity, complete 195 Pt NMR spectra can be obtained with sensitivity far exceeding that offered by traditional methods. These schemes, together with DFT computations, were applied to unravel the molecular and electronic signatures of surface Pt species. The large variations in experimental 195 Pt CSA can be related to simple orbital models, rationalizing the effect of different coordination environments on 195 Pt CSA patterns.

A) Characterization of Pt metal sites



B) Benchmark and Molecular Precursors

C) Supported Single-Site Materials

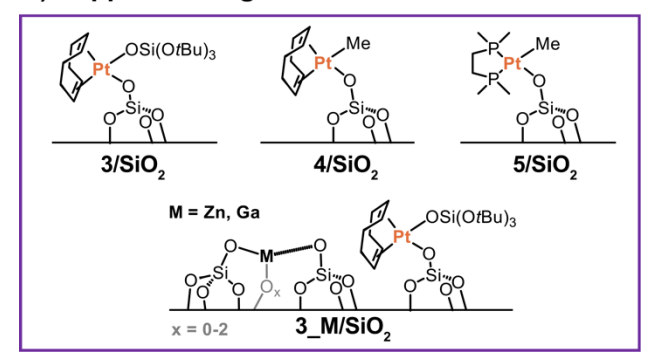


Figure 1. (A) Graphical summary of the characterization of molecular and supported Pt metal sites and the development of methodology for fast structure determination using ¹⁹⁵Pt solid-state NMR. Scheme showing the structures of the (B) molecular and (C) supported single-site Pt compound studied in this work. The Pt loadings of the supported compounds were 3.73 wt.% (3/SiO₂), 2.77 wt.% (3_Zn/SiO₂), 4.37 wt.% (3 Ga/SiO₂), 4.96 wt.% (4/SiO₂) and 4.39 wt.% (5/SiO₂).

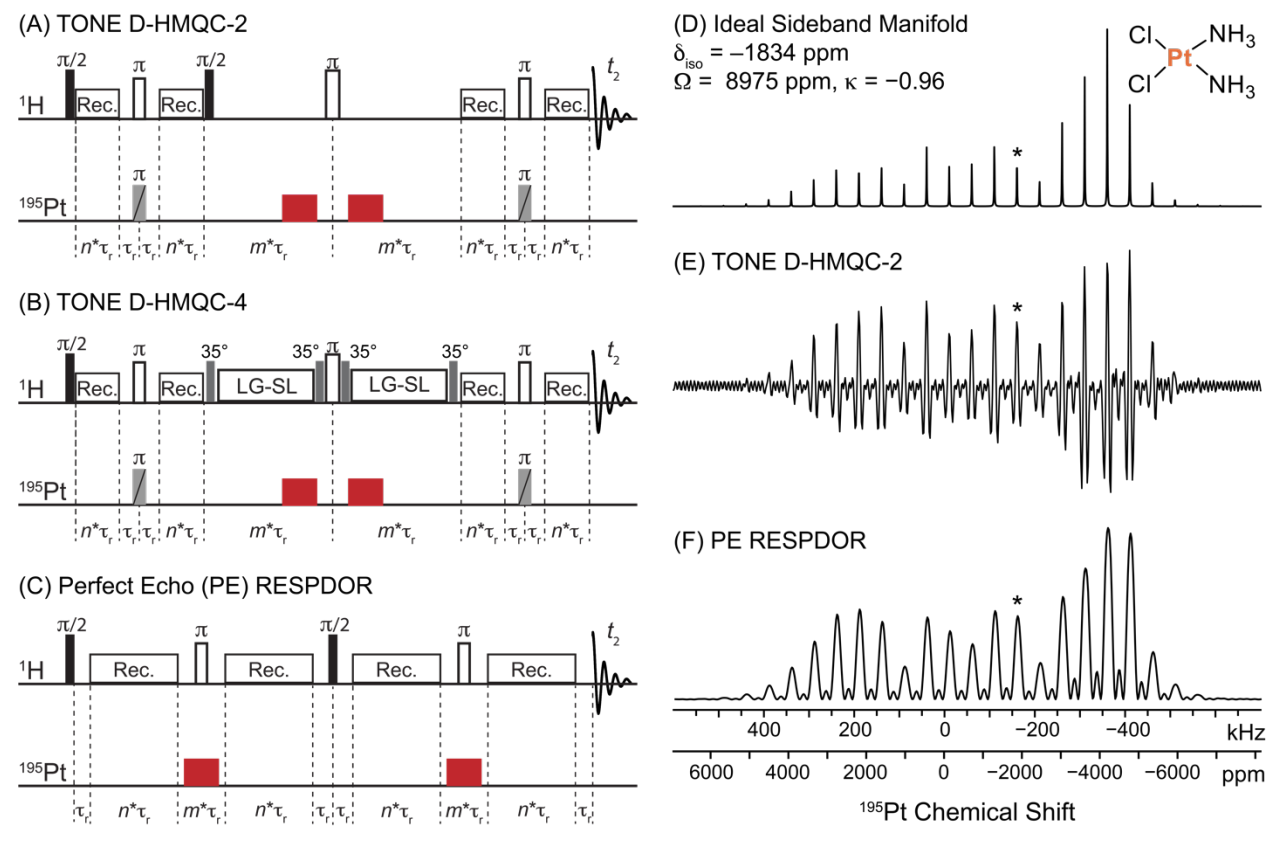


Figure 2. 1 H{ 195 Pt} (A) TONE D-HMQC-2, (B) TONE D-HMQC-4 and (C) Perfect echo (PE) RESPDOR pulse sequences with low-rf field, sideband-selective excitation/saturation pulses with durations of one or more rotor cycles on the 195 Pt channel denoted as red rectangles. m and n are positive integers and τ_r denotes a rotor period. (D-F) Simulations of MAS 195 Pt NMR spectra of cisplatin at 50 kHz MAS and $B_0 = 9.4$ T using the previously reported 195 Pt isotropic shift and CSA parameters (span (Ω) and skew (κ)). (D) Ideal simulation. Numerical SIMPSON simulations of sideband intensities obtained by varying the offset in steps of 1 kHz of 60 μs 195 Pt sideband-selective (9 kHz rf field) excitation or saturation pulses within (E) TONE D-HMQC or (F) PE RESPDOR pulse sequences, respectively. The isotropic shift is indicated by an asterisk.

Results and Discussion

Sideband-Selective ¹⁹⁵Pt NMR methods. Wideline ¹H{¹⁹⁵Pt} D-HMQC experiments⁷¹⁻⁷⁴ use microsecond duration, high-rf field ($v_1 > 150 \text{ kHz}$) excitation pulses to excite the broad ¹⁹⁵Pt NMR spectra. Small rotor-asynchronous t_1 -increments ($\Delta t_1 < 4 \mu s$) are used to finely sample the indirect dimension time domain signal, allowing observation of the entire wideline ¹⁹⁵Pt MAS spectrum in the frequency domain after 2D Fourier transformation.⁷¹⁻⁷⁴ However, when the indirect dimension spectrum consists of a series of sidebands due to a significant CSA, the sensitivity of the wideline NMR experiment is significantly reduced (Figure S1), and further

attenuated by t_1 -noise. Recently Paluch $et\ al.$ showed that the traditional microsecond duration, high-rf field excitation pulses used in ${}^1H\{^{195}Pt\}$ D-HMQC experiments on samples with large CSA can be replaced with low-rf field pulses (5-50 kHz) with durations of one rotor cycle or longer. These multiple rotor cycle duration pulses have a narrow excitation bandwidth and must be applied on resonance with an isotropic peak or sideband; hence, we denote these pulses as being sideband-selective. Here, sideband-selective excitation or saturation ${}^{195}Pt$ pulses are incorporated into D-HMQC and RESPDOR pulse sequences. To obtain the MAS ${}^{195}Pt$ solid-state NMR spectra, a series of 1D sideband-selective D-HMQC or RESPDOR experiments are performed where the ${}^{195}Pt$ pulse offset frequency is stepped in increments equal to the MAS frequency. By plotting the 1D NMR signal intensities as a function of the ${}^{195}Pt$ pulse offset the MAS ${}^{195}Pt$ NMR spectrum can be reconstructed (Figure 2 and Figure S2-S4). This method is analogous to previous work that utilized indirect detection schemes such as TRAPDOR, ${}^{76-77}$ REAPDOR, 78 RESPDOR ${}^{79-80}$ or PROSPR 81 where the signal dephasing of the detected nucleus at different transmitter offsets was used to reconstruct the NMR spectrum of the indirectly detected spin.

Figure 2D shows the simulated ideal MAS ¹⁹⁵Pt NMR spectrum of cisplatin, based on the previously reported CSA parameters $\delta_{iso} = -1834$ ppm, $\Omega = 8975$ ppm and $\kappa = -0.96$, $^{60, 71}$ where δ_{iso} , Ω and κ denote the isotropic chemical shift, span and skew of the chemical shift tensor, respectively. Numerical SIMPSON⁸²⁻⁸⁴ simulations show the effects of varying the offset of 60 μ s, 9 kHz rf field ¹⁹⁵Pt pulses in 2 kHz steps for the TONE D-HMQC-2 and PE RESPDOR pulse sequences with $SR4_1^2$ recoupling⁸⁵ (Figure 2E and 2F). Most importantly, a comparison of Figure 2E and 2F with Figure 2D shows that the MAS ¹⁹⁵Pt NMR spectrum is essentially reproduced in both cases, with peak intensities obtained with the PE RESPDOR sequence being very similar to the ideal spectrum (Figure 2D). Further details on sideband-selective NMR experiments and

simulations are found in the SI for the interested reader (Figure S5-S11, Note S1), and will be elaborated on in a forthcoming publication. Note that the simulations and experiments shown in Figure 2 and 3 used t_1 -noise eliminated (TONE) D-HMQC⁸⁶ and the closely related perfect echo⁸⁷ (PE) RESPDOR pulse sequences (Figure 2). Both of these sequences give more reliable ¹H NMR signal intensities because they are designed to tolerate experimental MAS frequency fluctuations.^{86, 88-89} The use of PE RESPDOR to accurately measure heteronuclear distances is discussed elsewhere.⁹⁰

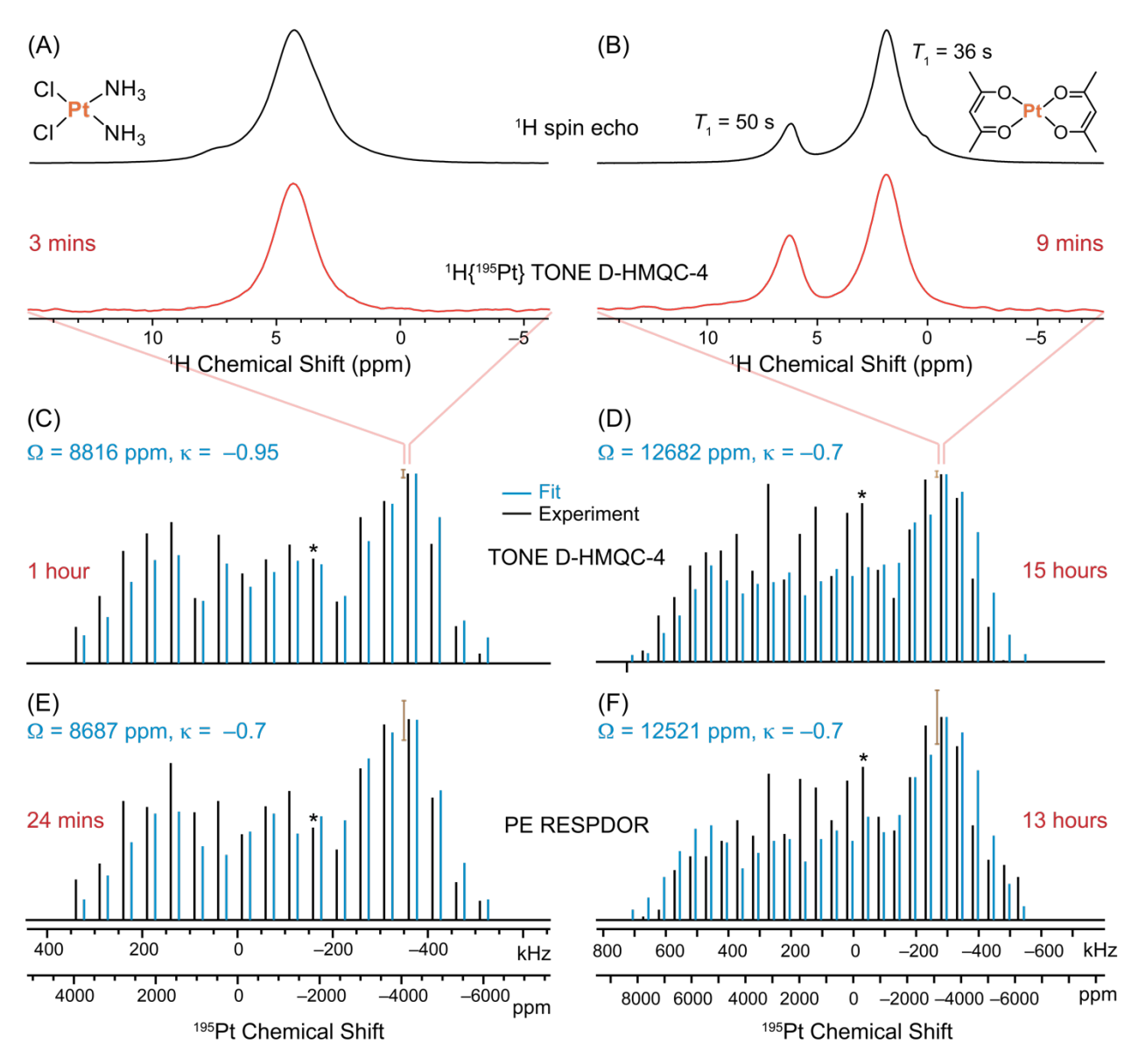


Figure 3. (A-B, upper traces) 1D ¹H spin echo spectra. (A-F) ¹H{¹⁹⁵Pt} sideband-selective solid-state NMR experiments on (A, C, E) cisplatin (1) and (B, D, F) Pt(acac)₂ (2) performed with a 50 kHz MAS frequency. (A-B, lower traces) 1D ¹H{¹⁹⁵Pt} sideband-selective TONE D-HMQC-4 with the ¹⁹⁵Pt transmitter applied at the most-intense sideband. (black traces) Sideband intensities from ¹H{¹⁹⁵Pt} (C-D) TONE D-HMQC-4 and (E-F) PE RESPDOR experiments using 60 μs, 9 kHz rf field sideband-selective ¹⁹⁵Pt pulses. For 2, the signal intensities of the CH proton at 6.3 ppm are shown. (blue traces) SIMPSON simulated peak intensities corresponding to the indicated CS tensor parameters which gave the lowest RMSD. Error bars are provided only for the most intense sideband as the same magnitude of error applies to all sidebands (see SI for details on error bars). Total experiment times are indicated in red.

Experimental Demonstration of ¹⁹⁵Pt Sideband-Selective NMR Experiments on Molecular Precursors. We tested sideband-selective ¹H{¹⁹⁵Pt} TONE D-HMQC-4 and PE RESPDOR experiments with the two prototypical molecular compounds cisplatin (1) and Pt(acac)₂ (2) (Figure

3). The sideband-selective pulses must be applied precisely on-resonance with a ¹⁹⁵Pt NMR signal. The position of a sideband can be located using a high sensitivity rotor-synchronized D-HMQC experiment^{66, 73, 75} or by varying the offset of the sideband-selective pulses in steps of 1-2 kHz, until the signal (or dephasing) is observed; the former approach was employed throughout this work. For both 1 and 2, plots of the ¹H{¹⁹⁵Pt} TONE D-HMQC-4 signal or the PE RESPDOR dephasing as a function of the sideband-selective pulse offset yields the intensity of each sideband in the MAS ¹⁹⁵Pt NMR spectrum.

For both types of NMR experiments CSA parameters were determined by least-squares fitting of the sideband intensities using SIMPSON simulations (Figure S12). The resulting CSA parameters obtained with sideband-selective ${}^{1}H\{{}^{195}Pt\}$ TONE D-HMQC-4 for **1** (Ω = 8816 ppm, κ = -0.95) are in close agreement with the known values (Ω = 8975 ppm, κ = -0.96). 60,71 Analysis of the sideband-selective PE RESPDOR data set yields Ω = 8687 ppm and κ = -0.7, again in good agreement with the established CSA tensor parameters (Figure S11C).

¹H{¹⁹⁵Pt} sideband-selective NMR experiments were also applied to **2**, which has not previously been analyzed by ¹⁹⁵Pt solid-state NMR. The 1D ¹H solid-state NMR spectrum of **2** showed two signals at 1.9 and 6.3 ppm, corresponding to the methyl and CH hydrogen atoms of the acetylacetonate ligands, respectively (Figure 3B). A standard 1D ¹H{¹⁹⁵Pt} TONE D-HMQC-2 spectrum showing both ¹H NMR signals can be obtained in a few minutes (Figure 3B), despite the long ¹H *T*₁ (36 and 50 s for the methyl and methine ¹H, respectively) and small ¹H-¹⁹⁵Pt heteronuclear dipolar couplings of ca. 300 Hz (see ¹H{¹⁹⁵Pt} SHAP S-REDOR experiments^{66, 74} in Figure S13A). Rotor-synchronized 2D TONE D-HMQC-4 experiments were performed with MAS frequencies of 50 and 52 kHz to measure the ¹⁹⁵Pt isotropic chemical shift of **2** (Figure S13B). Notably, two ¹⁹⁵Pt signals at –360 and –385 ppm were observed, suggesting that the sample

studied here contains two crystallographically inequivalent sites, in disagreement with the currently known crystal structure of 2.91 A 13C CPMAS spectrum of 2 also shows more peaks than expected, yet the experimental PXRD pattern closely matches that predicted from the 200 K Xray structure (Figure S13). Hence, we conclude that the sample of 2 studied here was phase pure, but that the structure at room temperature may be slightly different from the reported 200 K singlecrystal X-ray structure. A wideline ¹H{¹⁹⁵Pt} D-HMQC experiment on 2 takes 45 hours and it suffers from an incomplete excitation because of the large CSA (Figure S13C). The Ω was estimated to be 11800 ppm (Figure S13D, Note S2), in good agreement with a previous estimate of 10000 ppm from solution ¹⁹⁵Pt NMR relaxation experiments.⁹² On the other hand, with sideband-selective TONE D-HMQC-4 and PE RESPDOR experiments, ¹⁹⁵Pt NMR spectra were obtained in only 15 and 13 hours, respectively (Figure 3). Fits of the ¹⁹⁵Pt NMR spectra obtained with TONE D-HMQC-4 or PE RESPDOR yielded a κ of -0.7 and similar Ω values of 12682 ppm or 12521 ppm (Figure S14), which agree with the parameters determined from the MAS ¹⁹⁵Pt NMR spectrum extracted from the ¹H{¹⁹⁵Pt} D-HMQC experiment (Figure S13D). Resolving the two CSA patterns for the two platinum sites of 2 is not possible under our experimental conditions because of their similar isotropic shifts (ca. 15 ppm and 2150 Hz isotropic shift difference).

In summary, the sideband-selective ¹H{¹⁹⁵Pt} TONE D-HMQC and PE RESPDOR experiments were performed with unprecedented sensitivity: the entire ¹⁹⁵Pt MAS NMR spectrum of cisplatin was obtained in only 1 hour with TONE D-HMQC-4 and 24 minutes with PE RESPDOR. For Pt(acac)₂ the ¹⁹⁵Pt MAS NMR spectrum was obtained within 15 hours, despite the unfavorable NMR properties of **2**. Given the high signal to noise ratios observed with cisplatin (Figure S15), preliminary ¹⁹⁵Pt MAS NMR spectra can typically be obtained in a few minutes for most pure compounds. With these remarkable first results on molecular compounds, sideband-

selective ¹H{¹⁹⁵Pt} solid-state NMR experiments were then applied to examine silica-supported platinum compounds.

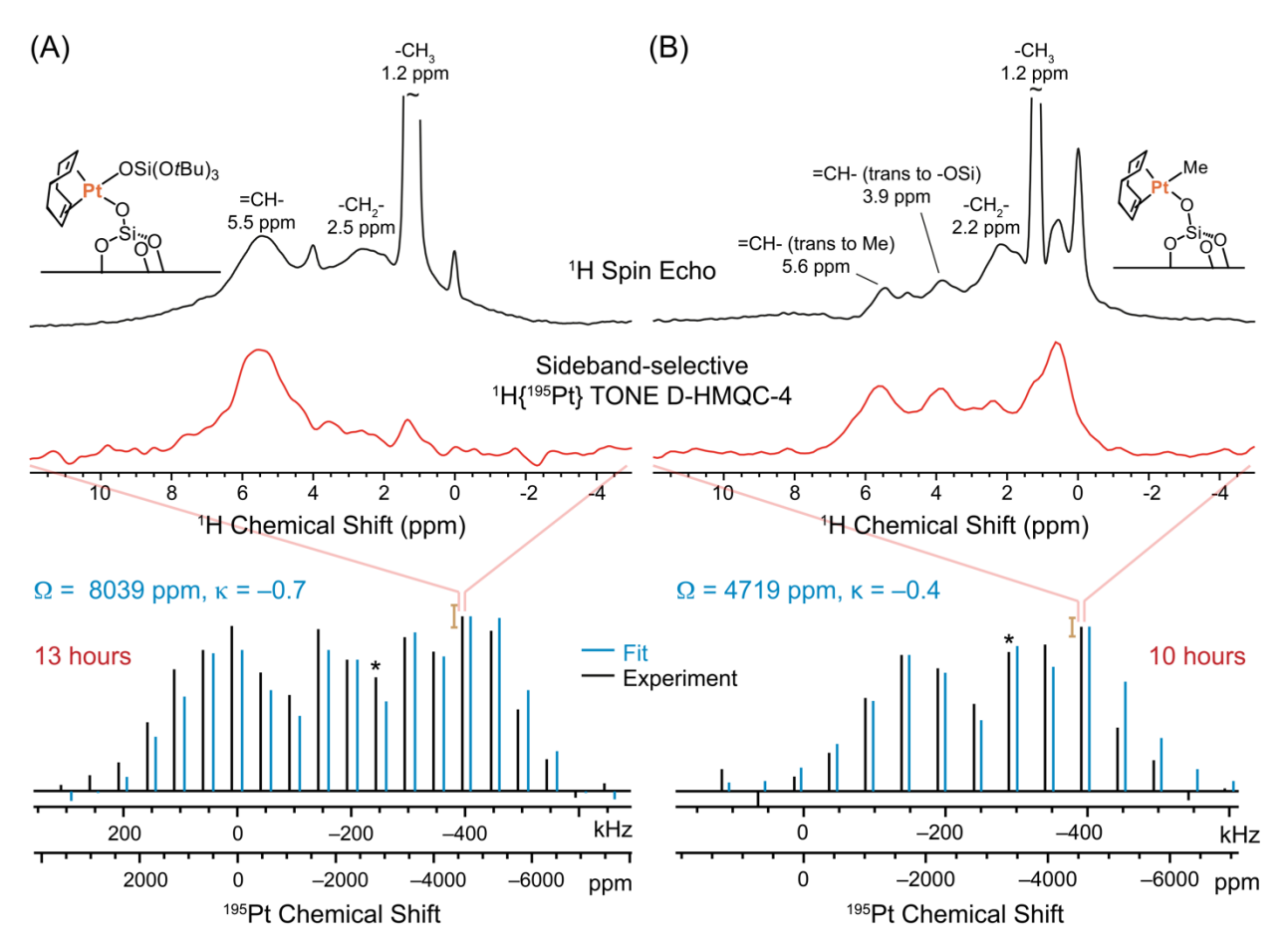


Figure 4. ¹⁹⁵Pt sideband-selective NMR experiments with silica-supported Pt compounds (A) **3/SiO**₂ and (B) **4/SiO**₂. (top) 1D ¹H spin echo NMR spectra, (middle) sideband-selective ¹H{¹⁹⁵Pt} TONE D-HMQC-4 spectra at the indicated ¹⁹⁵Pt offset (corresponding to the most intense sidebands). (bottom, black trace) ¹H{¹⁹⁵Pt} sideband-selective TONE D-HMQC-4 spectra of (A) **3/SiO**₂ and (B) **4/SiO**₂, obtained from the intensities of the CH ¹H NMR signal at ca. 5.5 ppm and the CH₃ ¹H NMR signal at 1.2 ppm, respectively. (blue trace) SIMPSON simulations with TONE D-HMQC-2 using ¹⁹⁵Pt (A) Ω = 8039 ppm, κ = -0.7 and (B) Ω = 4719 ppm, κ = -0.4, which correspond to the CS tensors parameters that give the lowest RMSD. The error bar accounting for SNR is shown for the most intense sideband. Intense *t*-butoxide methyl signals were truncated in the ¹H spin echo NMR spectra. All experiments were performed with a 50 kHz MAS frequency.

MAS ¹⁹⁵Pt Solid-State NMR of Surface Species. In order to investigate materials used in heterogeneous catalysis, we first measured the ¹⁹⁵Pt CSA of a model single-site compound prepared by grafting 3 [(COD)Pt(OSi(OtBu)₃)] on partially dehydroxylated silica^{12, 49, 93} which

yields (3/SiO₂) with a surface Pt loading of 3.73 wt.% (ca. 1 Pt/nm²). Recently, we determined the CS tensor parameters of $3/\text{SiO}_2$ ($\delta_{iso} = -2819$ ppm, $\Omega = 8412$ ppm, $\kappa = -0.77$) using a combination of DNP-SENS ¹H→¹⁹⁵Pt BRAIN-CP WCPMG and isotropic fast MAS ¹H-¹⁹⁵Pt TONE D-HMQC experiments that required approximately five days and one day of spectrometer time, respectively. 66 As we showed previously, the 195Pt isotropic peak and sidebands of the grafted compound are broad (ca. 8-10 kHz full width at half maximum) because of an inhomogeneous distribution of isotropic shifts likely related to slightly different local environments, a result from the amorphous character of silica.⁶⁶ To enable efficient excitation/saturation in the sidebandselective experiments, 40 µs excitation pulses with an optimal rf field of 16 kHz were used (Table S1, Figure S3-S4). The sideband-selective TONE D-HMQC-4 experiment yielded the MAS ¹⁹⁵Pt CSA pattern within 13 hours that could be fitted to $\Omega = 8039$ ppm, $\kappa = -0.7$, consistent with the reported values mentioned above (Figure 4A and Figure S16-S17). Although PE RESPDOR showed only a maximum dephasing of 5% (corresponding to an estimated error of ca. 20% of the dephasing difference signal intensities), a ¹⁹⁵Pt NMR spectrum was obtained in only 3.3 hours and fits of this spectrum gave $\Omega = 7876$ ppm, $\kappa = -0.8$ (Figure S17). The significant savings in time (few hours) compared to our previous report (6 days), 66 demonstrates the high sensitivity of the sideband-selective experiments for measurement of ¹⁹⁵Pt NMR spectra.

To probe if the sideband-selective experiments are suitable to detect differences in the ligand environment of supported compounds, we obtained ¹⁹⁵Pt NMR spectra of [(COD)PtMe]/SiO₂ (4/SiO₂) that has a surface Pt loading of 4.96 wt.%. In 4/SiO₂, the –OSi(OtBu)₃ ligand of 3/SiO₂ is replaced with a methyl ligand. Consequently, in 4/SiO₂ the two sets of olefinic protons in the COD ligand become inequivalent; the CH protons *trans* to the methyl and –OSi groups appear at 5.6 and 3.9 ppm, respectively, in close accordance with the solution ¹H NMR

spectrum of 4 ($\delta_{iso} = 5.90$ and 3.56 ppm, Figure S18). As a result, the signal intensities of the olefinic protons is halved in comparison to 3/SiO₂ which will decrease the overall indirect detection sensitivity. However, the methyl group protons at 1.2 ppm are also in close proximity to the Pt center and can also be used as spy nuclei for the indirect detection experiments. Indeed, all of these ¹H NMR signals are clearly observed in rotor-synchronized 1D and 2D ¹H{¹⁹⁵Pt} TONE D-HMQC-2 spectra (Figure 4B, Figure S19), indicating that COD and methyl ligands remain coordinated to Pt after grafting on silica. For $4/SiO_2$ δ_{iso} was determined to be -3327 ppm from the rotor-synchronized 2D ¹H{¹⁹⁵Pt} TONE D-HMOC-2 spectra (Figure S19). A single 1D sideband-selective ¹H{¹⁹⁵Pt} TONE D-HMQC-4 spectrum can be acquired in only 40 minutes with a SNR of 20 at the most intense sideband. Consequently, the entire ¹⁹⁵Pt MAS NMR spectrum of 4/SiO₂ was obtained in only 10 hours (Figure 4B). Least-squares fitting of the resulting pattern with SIMPSON simulations provides $\Omega = 4719$ ppm, $\kappa = -0.7$ (Figure S20), which illustrates a significant lowering of the span in comparison to 3/SiO₂. These results demonstrate that the new solid-state NMR experiments are well suited to capture differences in Pt environments of surface species.

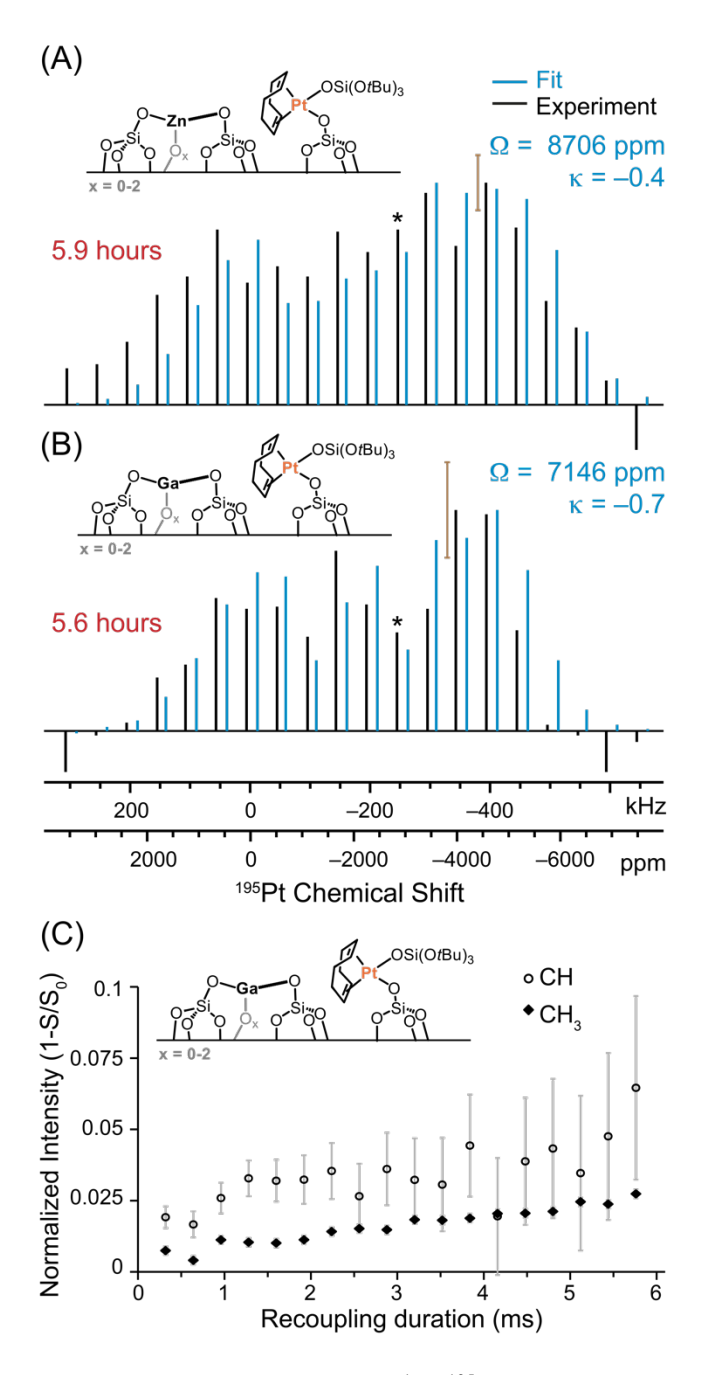


Figure 5. Sideband-selective ¹H{¹⁹⁵Pt} PE RESPDOR experiments on single-site Pt compounds (A) **3_Zn/SiO**₂ and (B) **3_Ga/SiO**₂. (black) Experimental patterns and (blue) SIMPSON simulations performed using the indicated CS tensor parameters. A maximum experimental signal dephasing of (A) 6.4% and (B) 3.7% was observed. Error bars are shown for the most intense sidebands. (C) ¹H{⁷¹Ga} PE RESPDOR build-up curves: plot showing normalized dephasing difference signal intensity (1–*S/S*₀) as a function of dipolar recoupling duration for (circles) CH and (diamonds) CH₃ groups in the grafted [(COD)Pt(OSi(O*t*Bu)₃)] complex.

In order to probe the sensitivity of these newly developed NMR experiments to modifications on the surface, we investigated the surface species of $[(COD)Pt(OSi(OtBu)_3)_2]$

grafted on silica doped with different Lewis acids, namely Zn(II) and Ga(III), in order to probe the local environment around Pt and determine if there are any interactions of Pt with the adjacent Lewis acid sites. These systems, denoted $3_{Zn/SiO_2}$ and $3_{Ga/SiO_2}$, were chosen because they are used as precursors to prepare highly active mixed-metal nanoparticle catalysts for the non-oxidative propane dehydrogenation.^{13, 15-16} The 1D ¹H NMR spectra of both compounds clearly show signals corresponding to CH₃ (ca. 1.2 ppm), CH₂ (ca. 2.2 ppm) and the olefinic CH (ca. 5.6 ppm) protons (Figure S21), in good agreement with the chemical shift assignments of $3/SiO_2$.⁶⁶ The ligand structure was further confirmed by 2D ¹H single quantum-double quantum (SQ-DQ) correlation spectroscopy, and ¹³C and ²⁹Si DNP-SENS (Figure S21-S23). Rotor-synchronized 2D ¹H{¹⁹⁵Pt} TONE D-HMQC spectra were used to measure the isotropic ¹⁹⁵Pt chemical shifts of – 2844 and –2828 ppm for $3_{Zn/SiO_2}$ and $3_{Ga/SiO_2}$, respectively (Figure S24). These isotropic shift values are entirely consistent with a similar Pt local environment as found in $3/SiO_2$ (¹⁹⁵Pt $\delta_{iso} = -2819$ ppm).

Figure 5A and 5B shows comparisons between experimental sideband patterns obtained with ${}^{1}H\{{}^{195}Pt\}$ PE RESPDOR and corresponding SIMPSON simulations using the best fit ${}^{195}Pt$ CS tensor parameters. Sideband-selective ${}^{1}H\{{}^{195}Pt\}$ PE RESPDOR was used to measure the ${}^{195}Pt$ MAS NMR spectra of ${\bf 3_Zn/SiO_2}$ and ${\bf 3_Ga/SiO_2}$ because it provided better sensitivity than TONE D-HMQC. We obtained $\Omega=8706$ ppm and $\kappa=-0.4$ for ${\bf 3_Zn/SiO_2}$ and $\Omega=7146$ ppm, $\kappa=-0.7$ for ${\bf 3_Ga/SiO_2}$, from least-squares fitting (Figure S25). Notably, the ${}^{195}Pt$ NMR spectra obtained with the sideband-selective experiments are clearly superior to those obtained with DNP-SENS ${}^{1}H \rightarrow {}^{195}Pt$ BRAIN-CP-WCPMG⁶² NMR experiments, which provided only partial excitation of the ${}^{195}Pt$ shielding patterns, with greatly reduced intensity at the high-frequency side of the pattern

(Figure S26). Note that similar distortions of intensity were previously seen in the $^{1}H\rightarrow^{195}Pt$ BRAIN-CP-WCPMG spectrum of $3/SiO_{2}$.

Clearly, the structure of the grafted single-site [(COD)Pt(OSi(OtBu)₃)] species in 3_Zn/SiO₂ is similar to 3/SiO₂. In case of 3_Ga/SiO₂, the observed ¹⁹⁵Pt sideband manifold indicates a span that is lower than that of 3/SiO₂ by ca. 1250 ppm, which could indicate differing interactions between the grafted Pt compounds and the co-grafted Ga³⁺ and Zn²⁺ ions, that in turn suggests slight average differences in the conformation and electronic structure. Note that the reduction in span of 3_Ga/SiO₂ could also be partially attributed to the error in intensities due to a low PE RESPDOR dephasing of ca. 3.7%. To confirm the proximity of the co-grafted Pt complex and the Ga³⁺ ions, we performed ¹H{⁷¹Ga} PE RESPDOR experiments which show dephasing of the olefinic CH and the methyl groups of the siloxide ligand (Figure 5C). The slow build-up of the ¹H{⁷¹Ga} PE RESPDOR curve is consistent with ¹H-⁷¹Ga inter-nuclear distances on the order of several angstroms. Similar RESPDOR experiments could not be performed on 3_Zn/SiO₂ due to the low ⁶⁷Zn natural abundance of 4.1%.

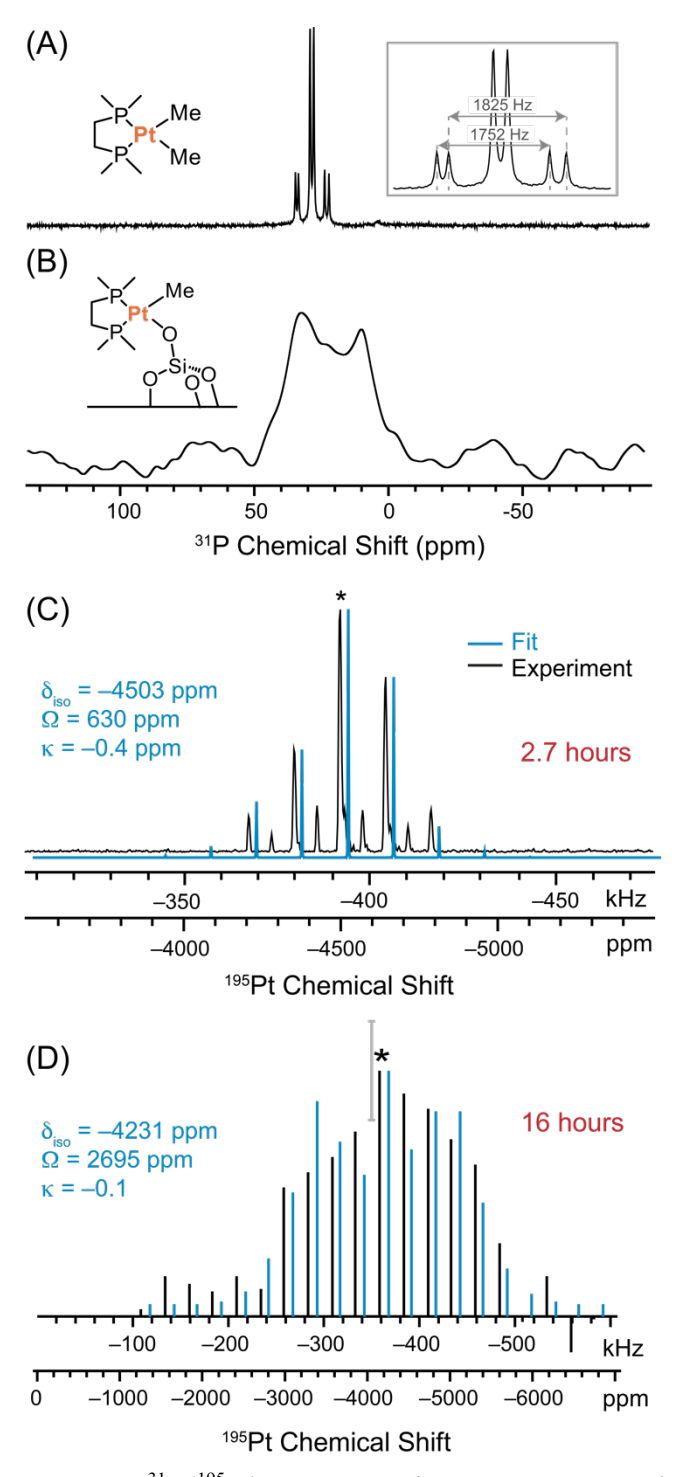


Figure 6. $^{31}P\{^{195}Pt\}$ NMR experiments on compounds **5** and **5/SiO₂**. $^{1}H\rightarrow^{31}P$ CP-MAS spectra of (A) **5** and (B) **5/SiO₂** obtained with a 25 kHz MAS frequency. (C) 1D ^{195}Pt projection from a 2D $^{31}P\{^{195}Pt\}$ CP constant time *J*-HMQC spectrum of **5** acquired with a 12.5 kHz MAS frequency. (D) ^{195}Pt CSA pattern of **5/SiO₂** acquired with a sideband-selective $^{1}H-^{31}P\{^{195}Pt\}$ CP *J*-resolved pulse sequence using CPMG detection and a 25 kHz MAS frequency.

³¹P{¹⁹⁵Pt} J-HMQC and J-Resolved NMR Experiments. While ¹H spins near ¹⁹⁵Pt were used to indirectly observe ¹⁹⁵Pt CSA patterns and determine the local structure of single-site Pt compounds, many catalysts can contain alternative ligands, such as phosphines. ³¹P can also serve as a spy nucleus for sideband-selective experiments as it offers good NMR sensitivity. We demonstrate this approach with [(DMPE)PtMe₂] (5) and the corresponding supported compound 5/SiO₂ (Figure 1) using *J*-based ¹H-³¹P{¹⁹⁵Pt} solid-state NMR experiments performed with a triple-resonance 2.5 mm HXY probe and MAS frequencies of 12.5 and 25 kHz, respectively.

Figure 6A shows a ${}^{1}\text{H} \rightarrow {}^{31}\text{P}$ CP-MAS spectrum of 5, which can be obtained within a few minutes. Two ${}^{31}\text{P}$ sites are observed at 29.1 ppm and 30.4 ppm with ${}^{1}J_{\text{P-Pt}}$ values of 1825 and 1750 Hz, respectively. Both the chemical shifts and ${}^{1}J_{\text{P-Pt}}$ values agree closely with previous solution NMR measurements. 94 Note that small variations in bond angles/lengths in the solid-state can create inequivalence and cause two ${}^{31}\text{P}$ NMR signals to be observed instead of one. A ${}^{31}\text{P}\{{}^{195}\text{Pt}\}$ constant-time *J*-HMQC experiment was then performed on 5 (Figure S27A). The constant-time format of the HMQC experiment enables arbitrary and large F_1 spectral widths necessary for the indirect detection of ${}^{195}\text{Pt}$ spinning sideband manifolds. 71 The resulting ${}^{195}\text{Pt}$ NMR spectrum was fit to CS tensor parameters of $\delta_{iso} = -4503$ ppm, $\Omega = 630$ ppm and $\kappa = -0.4$ (Figure 6C).

The ³¹P CP-MAS spectrum of **5/SiO**₂ has a low SNR (ca. 9 after 3.5 hours of acquisition) because of the low Pt surface loading of 4.4 wt % and signal broadening due to surface disorder (Figure 6B). Additionally, the ³¹P NMR spectrum of **5/SiO**₂ shows two characteristic features at 35 and 10 ppm, consistent with the inequivalence of the two phosphines in the grafted species: one is *trans* to a methyl (35 ppm), while the other is *trans* to a siloxide group (10 ppm). CPMG detection was used to accelerate all ³¹P{¹⁹⁵Pt} solid-state NMR experiments on **5/SiO**₂. Due to low sensitivity, it was not possible to perform a ³¹P{¹⁹⁵Pt} wideline *J*-HMQC experiment on **5/SiO**₂.

However, a rotor-synchronized ³¹P{¹⁹⁵Pt} J-HMQC spectrum showed that the ¹⁹⁵Pt isotropic chemical shift of 5/SiO₂ was -4231 ppm (Figure S27B, Figure S28). The ¹⁹⁵Pt CSA of 5/SiO₂ was then measured using a ³¹P{¹⁹⁵Pt} CP *J*-resolved (heteronuclear spin echo) experiment with 40 µs ¹⁹⁵Pt sideband-selective saturation pulses at 22 kHz rf field (Figure 6D). The dephasing observed for CPMG spikelets at 36 and 29 ppm was averaged to improve the SNR (Figure S29). With this approach, the sideband manifold could be obtained in only 16 hours. Least-squares fitting of the sideband manifold yields $\Omega = 2695$ ppm and $\kappa = -0.1$ (Figure 6D, Figure S30). Interestingly, the values of δ_{iso} for 5 and 5/SiO₂ only differ by 272 ppm, a small difference with respect to the large chemical shift range of 195 Pt. However, the value of Ω for $5/\text{SiO}_2$ is considerably larger than that measured for 5 (2695 vs 630 ppm), illustrating the importance of measuring CSA to probe the changes in the local Pt coordination environment upon grafting. The origin of the large difference in ¹⁹⁵Pt CSA is further discussed below. In conclusion, sideband-selective ³¹P{¹⁹⁵Pt} *J*-resolved experiments enabled acquisition of the ¹⁹⁵Pt NMR spectrum of 5/SiO₂ in only 16 hours, demonstrating that NMR-active nuclei other than ¹H can be used for indirect detection of ¹⁹⁵Pt NMR spectra.

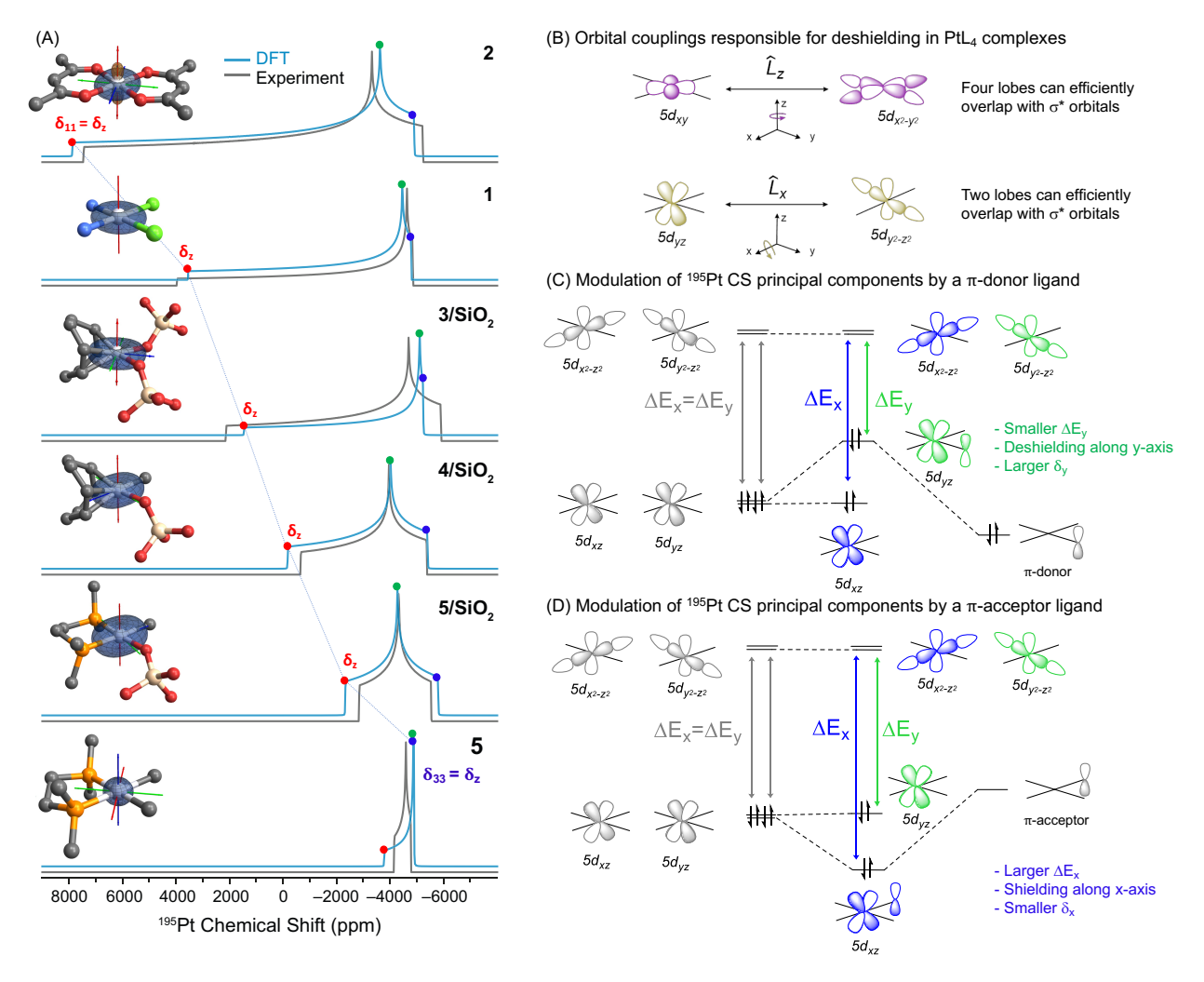


Figure 7. (A) Simulated static ¹⁹⁵Pt CSA parameters obtained using parameters from (black traces) sideband-selective NMR experiments and (blue traces) ZORA DFT calculations. The DFT optimized structures and the corresponding 3D representations of the calculated shielding tensors are shown for each compound. (B) Orbital couplings responsible for paramagnetic deshielding in square planar PtL₄ complexes. Modulation of orbital energies and Pt CS principal components in the plane by (C) a π-donor and (D) a π-acceptor ligand. In (A), blue and orange lobes indicate positive and negative shielding, respectively. The CSA principal components color code is: $\delta_{11} > \delta_{22} > \delta_{33}$. Plots of the shielding tensors are scaled to 0.002 pm/ppm. A summary of ¹⁹⁵Pt CSA parameters from different methods are provided in the Supporting Information in Table S2. NMR calculations of the supported species were performed using with *t*-butoxy siloxide groups in place of the silica surface. Hydrogen atoms are omitted for clarity. For the same reason, only the SiO₄ unit of the siloxide ligands is shown.

DFT Calculations of ¹⁹⁵Pt CS Tensors. Finally, we used spin-orbit ZORA DFT calculations to compute the ¹⁹⁵Pt CS tensor parameters of the molecular and supported Pt-species studied. ⁹⁵⁻⁹⁶ The differences in CSA parameters can be related to differences in the coordination environments using simple and powerful orbital models. Modern computational chemistry packages allow

accurate prediction of NMR properties, including ¹⁹⁵Pt chemical shifts, ^{58-59, 97} which is useful for structure determination by NMR crystallography protocols. ^{55, 98-99} As demonstrated by Ziegler, the origin of the ¹⁹⁵Pt CSA can be traced back to electronic structure. ¹⁰⁰ Autschbach subsequently demonstrated a localized molecular orbital analysis of ¹⁹⁵Pt CS tensors that provides a clear link between the energy and symmetry of orbitals in square planar Pt compounds and the observed CS tensor parameters: ^{55, 59} the deshielding for the CS component along the *z* direction of the molecular frame (denoted δ_z), originate from the coupling of the high-lying, filled d_{xy} orbital with the antibonding $\sigma^*(Pt-L)$ orbital by the $\hat{L_z}$ operator and, to a minor extent, from the filled d_{xz} and d_{yz} Pt orbitals coupling with the specific $\sigma^*(Pt-L)$ along the y or x axis, by $\hat{L_y}$ and $\hat{L_x}$ respectively (Figure 7B, details in experimental section below).

Standard gas-phase DFT calculations using the Gaussian09 program¹⁰¹ were used to optimize atomic coordinates. Then, ZORA DFT calculations as implemented in the ADF program¹⁰² were used to calculate ¹⁹⁵Pt CSA principal components ($\delta_{11} > \delta_{22} > \delta_{33}$) (for additional details, see the experimental section). The computed and experimental values of CSA are in good agreement, thus validating the computational approach (see Figure 7A and Table S2).

In all but one case, δ_{11} , the most deshielded component, lies perpendicular to the plane, along the natural z-axis of these square planar compounds ($\delta_{11} = \delta_z$). The exception is for compound 5, where δ_{33} is aligned with the molecular z-axis. Across the series of square planar compounds studied here, the value of δ_z varies from +7873 to -4885 ppm, while the other components in the plane (δ_x/δ_z), varies only within ca. 2000 ppm. Note also that small changes in geometry significantly affect ¹⁹⁵Pt CS tensor parameters (Figure S31).

The (de)shielding across the series of Pt-species studied here is clearly affected by the energy of $\sigma^*(Pt-L)$ orbitals, which is determined by the σ -donating properties of the corresponding

L ligands (Note S3). Thus, it may not be so surprising that changes in the coordination sphere of $Pt^{II}L_4$ compounds dramatically affect the δ_z component, which varies from +7873 (2) to -4885 ppm (5) upon going from oxygen to carbon-based ligands. As discussed above, the compound 5 presents the most shielded value for δ_z that correspond to δ_{33} and not δ_{11} as for the other compounds discussed here. Using the orbital-rotation model (Figure 7B, details in SI), one can readily justify the much more shielded value for δ_z in 5 which contains four strong σ -donor ligands bound to Pt (two methyl and two phosphine), hence the increase of $\sigma^*(Pt-L)$ orbital energies and high shielding of the Pt nucleus. At the opposite end, the compound 2 with acac ligands has four weak σ -donor oxygen atoms bound to Pt, leading to a lower $\sigma^*(Pt-L)$ orbital energy and the more deshielding δ_z (larger positive value). Overall, the strength of the σ -donating ligands drives the value of δ_z and determine the overall anisotropy and isotropic CS.

The sensitivity of the CS tensor parameters to the types of coordinated ligands explains why 5 and the supported $5/SiO_2$ have significantly different spans (Figure 7A). The replacement of one Pt-methyl bond in 5 by a Pt-siloxide bond in $5/SiO_2$ upon grafting, leads to a more deshielded δ_z component, as a result of the lower σ -donating properties of the siloxide ligand. This analysis also proves suitable to understand the differences in spans among supported Pt sites. For the supported species $3/SiO_2$ and $4/SiO_2$ the latter has a more shielded δ_z component, resulting from the presence of a methyl group, a strong σ -donor ligand. A remarkable difference in δ_z can also be observed between $4/SiO_2$ and $5/SiO_2$, where a more shielded δ_z in the latter can be related to the stronger σ -donating properties of DMPE with respect to the COD ligand.

Although CSA parameters in square planar $Pt^{II}L_4$ complexes are mostly affected by σ -interactions, the other principal components lying in the plane can be modulated through π -bonding interactions. These effects are observed upon comparison of $3/SiO_2$ with the respective asymmetric

complex 4/SiO₂. While the symmetric molecular model for 3/SiO₂ (having two siloxide ligands) has an axially symmetric CS tensor ($\delta_{22} \approx \delta_{33} \approx -5150$ ppm), the asymmetric system 4/SiO₂, with both a siloxide (weak π -donor) and a methyl ligand (mostly σ -donor) has δ_{22} (-4021 ppm) >> δ_{33} (-5400 ppm). In $4/\text{SiO}_2$, the most shielded component δ_{33} is aligned with the Pt-methyl bond, while δ_{22} is aligned with the Pt-siloxide bond. Specifically, the presence of a π -donor ligand causes an increase in energy of the overlapping filled Pt $5d_{yz}$ orbital through an antibonding interaction, which ultimately results in an increased energy of the $5d_{yz}$ orbital that allows for a more efficient coupling with $\sigma^*(Pt-L)$, hence the observed deshielding in the direction of the coupling (Figure 7C). On the contrary, a π -acceptor ligand can interact with the filled Pt $5d_{yz}$ orbital, stabilising it, and resulting in a less efficient orbital coupling due to increase in energy difference with the antibonding $\sigma^*(Pt-L)$ (Figure 7D). When combined, these orbital interactions lead to the observed effects in CSA of the asymmetric system 4/SiO₂; analogous observations can be made for 5/SiO₂. In summary, ¹⁹⁵Pt solid-state NMR spectra and CSA provide a signature of the metal sites, the types of ligands and the local symmetry of organometallic complexes and supported Pt species. Hence ¹⁹⁵Pt solid-state NMR spectroscopy is a powerful tool to characterize compounds and surface sites.

Conclusions

In conclusion, we have developed robust and expedient sideband-selective solid-state NMR methods to rapidly measure the ¹⁹⁵Pt NMR spectroscopic signatures of Pt-containing compounds and materials, including some having very large CSA such as Pt(acac)₂. The sideband-selective NMR experiments offer an enormous time saving in comparison to state-of-the-art static DNP SENS experiments. ⁶⁶ Additionally, the sideband-selective NMR methods can be performed

at room temperature and require only a few mg of material when performed with fast MAS probes and small diameter rotors. These methods are based on low-power pulses that are one or more rotor cycles in duration and provide sideband-selective excitation or saturation in fast MAS ¹H{¹⁹⁵Pt} TONE D-HMQC-4 and PE RESPDOR experiments, thus allowing the reconstruction of MAS ¹⁹⁵Pt sideband intensities from a series of 1D NMR spectra. This approach was also extended to sensitive spy nuclei such as ³¹P for indirect detection in sideband-selective ³¹P {¹⁹⁵Pt} *J*-resolved experiments, thus showing that, even in the absence of ¹H in the materials, other NMR active spy nuclei can be utilized to obtain valuable molecular-level information on metal sites. Furthermore, analysis of the CSA patterns down to the nature of the Pt-bonded ligands (σ -donor strength and π donating/accepting ability) provides an understanding of the trends in NMR parameters and also demonstrates the potential of Pt NMR spectroscopy to distinguish subtle differences in the Ptcoordination sphere. With this methodology in hand, we are currently exploring structurereactivity relationships in Pt-based single-atom catalysts, and are also investigating their applications to other high Z spin-1/2 nuclei with moderate isotopic abundance that exhibit large CSA. Finally, combining the sideband-selective NMR experiments with DNP should offer further gains in sensitivity that will be needed to study dilute single-atom catalysts or enable the use of nuclei such as natural abundance ¹³C as a spy-nucleus.

Experimental Section

Synthesis of Materials. All experiments were conducted inside an Argon filled MBraun GloveBox or using standard Schlenk technique, using anhydrous reagents and distilled solvents, unless indicated otherwise. All solvents were stored over 4 Å molecular sieves after being transferred to a glove box. Silica (SiO₂, Aerosil 200®, 200 m² g⁻¹) was calcined in air at 500°C

before subsequent dehydroxylation at 700°C under high vacuum as reported in literature. 10 The resulting dehydroxylated silica is referred to as SiO₂₋₇₀₀. Titration of the resulting SiO₂₋₇₀₀ using [Mg(CH₂Ph)₂(THF)₂] purified via sublimation prior to use, ¹⁰³ yielded an Si-OH density of 0.3 mmol/g, corresponding to 0.9 accessible Si-OH groups per nm². PtCl₂(NH₃)₂ (1, 99 % purity, Alfa Aesar) and Pt(acac)₂ (2, 98 % purity, Strem Chemicals) were used as received. $[(COD)Pt(OSi(O^tBu)_3)_2]$ (3),[(COD)PtMe(OSi(O^tBu)₃)] (4),[(DMPE)PtMe₂] (5),[Zn(OSi(OtBu)₃)₂]₂ and [Ga(THF)(OSi(OtBu)₃)₃] molecular precursors were synthesized via literature procedures with minor modifications. 12, 93, 104-106 [(COD)Pt(OSi(OtBu)₃)]/SiO₂ (3/SiO₂) was synthesized according to the previously described procedure.⁶⁶ The materials [(COD)Pt(OSi(OtBu)₃)] Zn^{II}/SiO₂ [(COD)Pt(OSi(OtBu)₃)] Ga^{III}/SiO₂ $(3 \text{ Zn/SiO}_2),$ (3 Ga/SiO₂) and [(COD)PtMe]/SiO₂₋₇₀₀ (4/SiO₂) were synthesized following adapted literature procedures. 12-13, 15

[(COD)Pt(OSi(OtBu)₃)] Zn^{II}/SiO₂ (3 Zn/SiO_2) : colourless solution of Α [Zn(OSi(OtBu)₃)₂]₂ (0.234 g, 0.395 mmol) in benzene (10 ml) was added slowly to a suspension of SiO₂₋₇₀₀ (1.517 g, 0.455 mmol -OH) in benzene (10 ml) while stirring (100 rpm). The resulting suspension was stirred for 5 h at room temperature. The supernatant was removed, and the material washed with benzene (10 ml) three times to wash off unreacted complex. The material was then washed with pentane and subsequently dried under high vacuum (10⁻⁵ mbar) for 3 h to remove residual solvent. The resulting white solid was then transferred to a tubular quartz reactor and treated under high vacuum (10⁻⁵ mbar) at high temperature (r.t. to 300 °C (5 °C/min) for 1 h, 400 °C (5 °C/min) for 1 h, 500 °C (5 °C/min) for 1 h, 600 °C (5 °C/min) for 8 h). Part of the resulting white solid (1.193 g, 0.358 mmol -OH assumed) was suspended in benzene (10 ml), and a colourless solution of 3 (0.258 g, 0.311 mmol) in benzene (10 ml) added to it slowly while stirring

(100 rpm). The resulting suspension was stirred for 4 h at room temperature. The supernatant was removed, and the material washed with benzene (10 ml) three times to wash off unreacted complex. The material was then washed with pentane and subsequently dried under high vacuum (10⁻⁵ mbar) for 3 h to remove residual solvent. **3_Zn/SiO₂** was obtained as a white solid. Elemental Analysis: 2.77 wt.% Pt, 1.48 wt.% Zn.

[(COD)Pt(OSi(OtBu)₃)] Ga^{III}/SiO_{2-700} (3_Ga/SiO₂): A colourless solution of [Ga(THF)(OSi(OtBu)₃)₃] (0.245 g, 0.263 mmol) in benzene (10 ml) was added slowly to a suspension of SiO₂₋₇₀₀ (1.009 g, 0.303 mmol -OH) in benzene (10 ml) while stirring (100 rpm). The resulting suspension was stirred for 12 h at room temperature. The supernatant was removed, and the material washed with benzene (10 ml) three times to wash off unreacted complex. The material was then washed with pentane and subsequently dried under high vacuum (10⁻⁵ mbar) for 5 h to remove residual solvent. The resulting white solid was then transferred to a tubular quartz reactor and treated under high vacuum (10⁻⁵ mbar) at high temperature (r.t. to 300 °C (5 °C/min) for 1 h, 400 °C (5 °C/min) for 1 h, 500 °C (5 °C/min) for 1 h, 600 °C (5 °C/min) for 8 h). Part of the resulting grey solid (0.480 g, 0.144 mmol –OH assumed) was suspended in benzene (10 ml), and a colourless solution of 3 (0.104 g, 0.125 mmol) in benzene (10 ml) added to it slowly while stirring (100 rpm). The resulting suspension was stirred for 12 h at room temperature. The supernatant was removed, and the material washed with benzene (10 ml) three times to wash off unreacted complex. The material was then washed with pentane and subsequently dried under high vacuum (10⁻⁵ mbar) for 3 h to remove residual solvent. **3 Ga/SiO₂** was obtained as a white solid.

[(COD)PtMe]/SiO₂₋₇₀₀ (4/SiO₂): A colourless solution of 4 (0.087 g, 0.15 mmol) in benzene (10 mL) was added slowly to a suspension of SiO₂₋₇₀₀ (0.500 g, 0.15 mmol -OH) in benzene (10 mL) while stirring (100 rpm). The resulting suspension was stirred for 12 h at room

temperature. The supernatant was removed, and the material washed with benzene (10 mL) three times to wash off unreacted complex. The material was then washed with pentane and dried under high vacuum (10⁻⁵ mbar) for 4 h to remove residual solvent. **4/SiO₂** was obtained as a white solid. Elemental analysis: Pt, 4.96 wt. %.

[(DMPE)PtMe]/SiO₂₋₇₀₀ (5/SiO₂): A suspension of off-white/brown **5** (0.035 g, 0.093 mmol) in benzene (10 mL) was added slowly to a suspension of SiO₂₋₇₀₀ (0.311 g, 0.093 mmol –OH) in benzene (10 mL) while stirring (100 rpm). The resulting suspension was stirred for 12 h at room temperature with gradual disappearance of **5** in the suspension. The supernatant was removed, and the material washed with benzene (10 mL) three times to wash off unreacted complex. The material was then washed with pentane and dried under high vacuum (10⁻⁵ mbar) for 2 h to remove residual solvent. **5/SiO₂** was obtained as a white solid. Elemental analysis: 4.39 wt.% Pt; 1.35 wt.% P.

Molecular DFT Calculations. Atomic coordinates were optimized with DFT using Gaussian09. The Calculations were performed using the B3LYP functional functional function with Pople's 6-31G(d) basis sets for H, C, Si atoms and 6-31+G(d) for negatively charged atoms (P, O). The Los Alamos LANL2TZ basis set was used for Pt atoms in conjunction with the associated pseudopotential. MRR calculations were performed using ADF 2016 with the PBE0 functional and Slater-type basis sets of quadruple-ζ quality (QZ4P) for Pt and triple-ζ quality (TZP) for other atoms. Relativistic effects were treated by the 2-component zeroth order regular approximation (ZORA). Secondary functional shifts were referenced to (COD)PtCl₂, with an experimental isotropic chemical shift of -3360 ppm, and a calculated isotropic shielding of 5483 ppm. Calculated shielding tensors are plotted as 3D representations of $\sum_{ij} r_i s_{ij} r_j$, polar functions with scaling factors adjusted towards the best readability. The calculated shielding tensors are plotted as 3D representations of $\sum_{ij} r_i s_{ij} r_j$, polar functions with scaling factors adjusted towards the best readability.

While the chemical shift (δ) is always reported with respect to a reference compound, DFT calculations output the magnetic shielding with respect to the bare nucleus (σ); the equation below is used to convert calculated shielding values to chemical shift values, which are ordered so that $\delta_{11} > \delta_{22} > \delta_{33}$.

$$\begin{pmatrix}
\delta_{11} & 0 & 0 \\
0 & \delta_{22} & 0 \\
0 & 0 & \delta_{33}
\end{pmatrix} = \sigma_{iso}^{ref} \begin{pmatrix} 1 & 0 & 0 \\
0 & 1 & 0 \\
0 & 0 & 1 \end{pmatrix} - \begin{pmatrix} \sigma_{11} & 0 & 0 \\
0 & \sigma_{22} & 0 \\
0 & 0 & \sigma_{33}
\end{pmatrix} \tag{1}$$

Plane-wave DFT Calculations. The hydrogen atom positions of $Pt(acac)_2$ in the previously reported crystal structure⁹¹ were optimized using plane-wave density functional theory (DFT). The CASTEP¹¹² program was used with the PBE-GGA functional¹¹³ and the TS dispersion correction scheme.¹¹⁴ A k-point spacing of 0.07 Å⁻¹ was used for the Monkhorst-Pack grid.

Solid-State NMR Experiments. All experiments were performed at 9.4 T using a Bruker Avance III HD console. ¹H, ³¹P and ¹⁹⁵Pt chemical shifts were indirectly referenced to tetramethylsilane using the ¹H shift of adamantane at 1.82 ppm. Analytical simulations were performed with the TopSpin solid lineshape analysis module (sola) or ssNake *v*1.1.¹¹⁵

Fast MAS ${}^{1}H\{^{195}Pt\}$ NMR Experiments. A Bruker 1.3 mm HX probe and the MAS frequency was 50 kHz unless mentioned otherwise. Cisplatin and L-histidine·HCl·H₂O were purchased and used as received from Alfa Aesar and Fluka, respectively; rotors of these samples were packed under ambient conditions. All other rotors were packed in an argon glovebox and rotors were spun with nitrogen gas. ${}^{1}H\{^{195}Pt\}$ TONE D-HMQC-4 and PE RESPDOR experiments were performed using $SR4_{1}^{2}$ dipolar recoupling⁸⁵ that was applied at the 2^{nd} order R^{3} condition. 116 ${}^{1}H$ 90° and 180° pulse durations of 2.5 and 5 μ s, respectively were used. The ${}^{195}Pt$ sideband-selective pulses were optimized by determining the rf fields that maximized D-HMQC signal

intensities using different pulse lengths (Table S1), with longer duration pulses providing more selectivity (Figure S3-S4). The ¹H{⁷¹Ga} PE RESPDOR experiment used 30 µs ⁷¹Ga saturation pulses with a 330 kHz rf field. In ¹H{¹⁹⁵Pt} TONE D-HMQC-4 experiments, SHAPs used tanh/tan shapes with a 20 µs duration, *ca.* 275 kHz rf field and 5 MHz sweep width. Lee-Goldburg spinlock pulses of ca. 1 ms total duration were applied at a rf field of 150 kHz at the appropriate transmitter offset frequency. ^{86, 117} For sideband-selective ¹H{¹⁹⁵Pt} TONE D-HMQC-4 experiments the ¹⁹⁵Pt offset for the SHAP inversion pulses was held constant, approximately in the center of NMR powder pattern, while the offset of the sideband-selective pulses was varied. For both TONE D-HMQC-4 and PE RESPDOR sideband-selective experiments the probe was not retuned for each offset. Retuning the probe was found to have a minimal effect on sideband intensities (Figure S5).

Total $SR4_1^2$ dipolar recoupling durations of 1.92 ms (1, TONE D-HMQC-4), 2.88 ms (1, PE RESPDOR), 3.2 ms (2, TONE D-HMQC-4 and PE RESPDOR), 1.76 ms (3/SiO₂, TONE D-HMQC-4), 2.08 ms (3/SiO₂, PE RESPDOR), 2.56 ms (4/SiO₂, TONE D-HMQC-4) and 2.4 ms (3_Zn/SiO₂ and 3_Ga/SiO₂, PE RESPDOR) were used in the various sideband-selective experiments. For the molecular compounds and silica-supported compounds 60 μ s, 9 kHz rf field and 40 μ s, 16 kHz rf field sideband-selective saturation pulses were employed, respectively. For 4/SiO₂ 40 μ s sideband-selective pulses with a 12 kHz rf field were used. In case of 1, although the maximum dephasing observed with PE RESPDOR was only ca. 9% with a total recoupling duration of 2.88 ms, the tolerance to MAS instability is higher at shorter recoupling durations (only 0.7% variation of the RESPDOR S_0 signal intensity was observed, which is the primary source of error in the measurements, Figure S7A). A longer recoupling duration provides more dephasing (Figure S7D) but results in a 'noisier' 195Pt sideband manifold (Figure S11). Therefore, recoupling

durations shorter than that providing maximal dephasing may be preferred for the variable offset PE RESPDOR experiments.

The experimental 195 Pt sideband-selective patterns are best reproduced by numerical simulations, as performed here using SIMPSON (*vide infra*). Alternatively, an approximate estimate of the CSA values can be obtained using Herzfeld-Berger analysis (HBA). $^{118-119}$ For example, with cisplatin, the isotropic shift was fixed to -1834 ppm while Ω and κ were fitted using the HBA program. The estimated CSA parameters for cisplatin were $\Omega = 9776$ ppm and $\kappa = -0.65$ with TONE D-HMQC-4, and $\Omega = 9584$ ppm and $\kappa = -0.64$ with PE RESPDOR (Figure S32). The HBA program used for fitting assumes ideal sideband intensities during fitting; however, the intensities of the 195 Pt pattern from the sideband-selective experiments deviate from the ideal pattern and can only be reproduced using numerical simulations. Therefore, HBA should be performed only to estimate the 195 Pt CSA.

Bruker 2.5 mm HXY probe. The pulse sequences used for the acquisition of ${}^{1}\text{H}$ - ${}^{31}\text{P}$ { ${}^{195}\text{Pt}$ } CP *J*-HMQC and sideband-selective *J*-resolved spectra are shown in Figure S27. Pulse durations of 2.5 μs ($\pi/2$, ${}^{1}\text{H}$), 4.75 μs (π , ${}^{31}\text{P}$) and 2-2.5 μs ($\pi/2$, ${}^{195}\text{Pt}$) were used. The constant-time 2D ${}^{1}\text{H}$ - ${}^{31}\text{P}$ { ${}^{195}\text{Pt}$ } CP *J*-HMQC spectrum of **5** was acquired with 12.5 kHz MAS, 8 scans, 1.5 s recycle delay (1.3× T_1), indirect spectral width of 500 kHz, 822 complex t_1 -increments and a total *J*-evolution time (2×m×τ_r) of 1.28 ms (Figure 6C). The ${}^{1}\text{H}$ - ${}^{31}\text{P}$ CP duration was set to 2.5 ms and optimal ${}^{1}\text{H}$ and ${}^{31}\text{P}$ spinlock rf powers of 75 kHz and 83 kHz, respectively, were used; the ${}^{1}\text{H}$ rf power was ramped from 85-100%. For all experiments with **5/SiO**₂, a ${}^{1}\text{H}$ - ${}^{31}\text{P}$ CP duration of 5 ms and optimal ${}^{1}\text{H}$ and ${}^{31}\text{P}$ spinlock rf powers of 105 kHz and 83 kHz, respectively, were used; the ${}^{1}\text{H}$ rf power was ramped from 90-100%. The sideband-selective ${}^{1}\text{H}$ - ${}^{31}\text{P}$ CP *J*-resolved

spectra of $5/SiO_2$ was acquired with 25 kHz MAS, 1800 scans and 1.5 s recycle delay per point; the total *J*-evolution time ($2 \times m \times \tau_r$) was set to 560 μ s, and a 40 μ s ¹⁹⁵Pt saturation pulse at 22 kHz rf was applied. The offset was incremented in steps of the MAS frequency and 21 sub-spectra were obtained. The total duration of each echo in the CPMG train was set to 800 μ s and 55 spin echoes were acquired. 100 kHz SPINAL-64 decoupling was applied during *J*-evolution periods and signal acquisition. ¹²⁰

SIMPSON simulations. All ¹H{¹⁹⁵Pt} SIMPSON simulations were performed with a 50 kHz MAS frequency and a ¹H Larmor frequency of 400.498 MHz. The ¹H-¹⁹⁵Pt dipolar coupling was set to -3500 Hz and an optimal recoupling duration of 2.88 ms was used. For the simulations shown in Figure 2, the rep168 crystal file and 24 gamma angles were used for powder averaging. For all other simulations in the main text, the rep320 crystal file and 13 gamma angles were used. 60 us selective excitation pulses with an optimized 9 kHz rf field were used in the simulations for all molecular compounds, whereas shorter 40 µs duration pulses at 16 kHz rf were used for the surface compounds. The optimal rf fields for the sideband-selective excitation pulses in D-HMQC agree well between simulations and experiments (Table S1). In all cases, the offset frequency of a sideband was determined by first varying the offset in small steps of 1-2 kHz, followed by stepping the transmitter offset in steps equal to the MAS frequency. Note that the TONE D-HMQC-2 sequence was used for SIMPSON simulations throughout this work, while TONE D-HMQC-4 was used for experiments. TONE D-HMQC-2 was used for simulations because TONE D-HMQC-4 relies on experimental rf inhomogeneity, which is absent in the simulations, to dephase uncorrelated signals. 86 The sideband-selective 31P {195Pt} J-resolved experiments with 5/SiO₂ were simulated using a ³¹P-¹⁹⁵Pt J-coupling of 1825 Hz, a *J*-evolution time of 560 µs, and a 25 kHz MAS frequency as in the experiments.

Plots showing the root mean square deviation (RMSD) between experimental and simulated patterns are provided in the SI for all samples. Briefly, the sideband NMR spectra were fit with the following procedure: (i) visual inspection of the sideband manifold provides a preliminary estimate of the principal components of the CSA tensor, (ii) the skew of the CS tensor was fixed while the span was varied and (iii) finally, the span with the lowest RMSD was fixed and the skew was varied to determine the best fit.

Acknowledgements

This work was primarily supported by a grant from the National Science Foundation CBET-1916809 to AJR. The development of sideband-selective NMR methods was supported by the U.S. Department of Energy (DOE), Office of Science, Basic Energy Sciences, Materials Science and Engineering Division. The Ames Laboratory is operated for the U.S. DOE by Iowa State University under contract # DE-AC02-07CH11358. AJR acknowledges additional support from the Alfred P. Sloan Foundation through a Sloan research fellowship. The research carried out at ETH Zürich was partially funded by the Swiss National Science Foundation (Grant number 200021_169134 and 200020B_192050). This work is part of a project that has received funding from the European Union's Horizon 2020 research and innovation programme under Grant Agreement No 101008500 ("PANACEA"). This work is also supported by the Common Research Laboratory CARMEN (ENS de Lyon, CNRS, IFPEN, Claude Bernard Lyon 1 University, Sorbonne University, and University of Strasbourg). We are grateful to Ribal Jabbour for his help with the setup of static ¹⁹⁵Pt solid-state NMR experiments. Dr. Christopher Gordon is also gratefully acknowledged for discussions on NMR computations.

Supporting Information

Additional experimental and simulated NMR spectra, and experimental details can be found in the supporting information. Pulse sequences, SIMPSON simulation input files, and raw NMR data for main text Figures are available for download at https://doi.org/10.5281/zenodo.6639016.

References

- 1. Bowker, M. *The Basis and Applications of Heterogeneous Catalysis*. Oxford University Press: Oxford, 1998.
- 2. Fechete, I.; Wang, Y.; Vedrine, J. C. The Past, Present and Future of Heterogeneous Catalysis. *Catal. Today* **2012**, *189* (1), 2-27.
- 3. Friend, C. M.; Xu, B. J. Heterogeneous Catalysis: A Central Science for a Sustainable Future. *Acc. Chem. Res.* **2017**, *50* (3), 517-521.
- 4. Coperet, C. Fuels and Energy Carriers from Single-Site Catalysts Prepared via Surface Organometallic Chemistry. *Nat. Energy* **2019**, *4* (12), 1018-1024.
- 5. Tennakoon, A.; Wu, X.; Paterson, A. L.; Patnaik, S.; Pei, Y. C.; LaPointe, A. M.; Ammal, S. C.; Hackler, R. A.; Heyden, A.; Slowing, I. I.; Coates, G. W.; Delferro, M.; Peters, B.; Huang, W. Y.; Sadow, A. D.; Perras, F. A. Catalytic Upcycling of High-Density Polyethylene via a Processive Mechanism. *Nat. Catal.* **2020**, *3* (11), 893-901.
- 6. Thomas, J. M.; Raja, R.; Lewis, D. W. Single-Site Heterogeneous Catalysts. *Angew. Chem. Int. Ed.* **2005**, *44* (40), 6456-6482.
- 7. Korzyński, M. D.; Copéret, C. Single Sites in Heterogeneous Catalysts: Separating Myth from Reality. *Trends Chem.* **2021**, *3* (10), 850-862.
- 8. Wang, A. Q.; Li, J.; Zhang, T. Heterogeneous Single-Atom Catalysis. *Nat. Rev. Chem.* **2018**, *2* (6), 65-81.
- 9. Wegener, S. L.; Marks, T. J.; Stair, P. C. Design Strategies for the Molecular Level Synthesis of Supported Catalysts. *Acc. Chem. Res.* **2012**, *45* (2), 206-214.
- 10. Coperet, C.; Comas-Vives, A.; Conley, M. P.; Estes, D. P.; Fedorov, A.; Mougel, V.; Nagae, H.; Nunez-Zarur, F.; Zhizhko, P. A. Surface Organometallic and Coordination Chemistry toward Single-Site Heterogeneous Catalysts: Strategies, Methods, Structures, and Activities. *Chem. Rev.* **2016**, *116* (2), 323-421.
- 11. Pelletier, J. D. A.; Basset, J. M. Catalysis by Design: Well-Defined Single-Site Heterogeneous Catalysts. *Acc. Chem. Res.* **2016**, *49* (4), 664-677.
- 12. Laurent, P.; Veyre, L.; Thieuleux, C.; Donet, S.; Coperet, C. From Well-Defined Pt(II) Surface Species to the Controlled Growth of Silica Supported Pt Nanoparticles. *Dalton Trans.* **2013**, *42* (1), 238-248.
- 13. Searles, K.; Chan, K. W.; Burak, J. A. M.; Zemlyanov, D.; Safonova, O.; Coperet, C. Highly Productive Propane Dehydrogenation Catalyst Using Silica-Supported Ga-Pt Nanoparticles Generated from Single-Sites. *J. Am. Chem. Soc.* **2018**, *140* (37), 11674-11679.
- 14. Coperet, C. Single-Sites and Nanoparticles at Tailored Interfaces Prepared via Surface Organometallic Chemistry from Thermolytic Molecular Precursors. *Acc. Chem. Res.* **2019**, *52* (6), 1697-1708.
- 15. Rochlitz, L.; Searles, K.; Alfke, J.; Zemlyanov, D.; Safonova, O. V.; Coperet, C. Silica-Supported, Narrowly Distributed, Subnanometric Pt-Zn Particles from Single Sites with High Propane Dehydrogenation Performance. *Chem. Sci.* **2020**, *11* (6), 1549-1555.
- 16. Payard, P. A.; Rochlitz, L.; Searles, K.; Foppa, L.; Leuthold, B.; Safonova, O. V.; Comas-Vives, A.; Copéret, C. Dynamics and Site Isolation: Keys to High Propane Dehydrogenation Performance of Silica-Supported PtGa Nanoparticles. *JACS Au* **2021**, *1* (9), 1445-1458.
- 17. Zhang, W. P.; Xu, S. T.; Han, X. W.; Bao, X. H. In Situ Solid-State NMR for Heterogeneous Catalysis: A Joint Experimental and Theoretical Approach. *Chem. Soc. Rev.* **2012**, *41* (1), 192-210.
- 18. D'Elia, V.; Dong, H. L.; Rossini, A. J.; Widdifield, C. M.; Vummaleti, S. V. C.; Minenkov, Y.; Poater, A.; Abou-Hamad, E.; Pelletier, J. D. A.; Cavallo, L.; Emsley, L.; Basset, J. M. Cooperative Effect of Monopodal Silica-Supported Niobium Complex Pairs Enhancing Catalytic Cyclic Carbonate Production. *J. Am. Chem. Soc.* **2015**, *137* (24), 7728-7739.
- 19. Kobayashi, T.; Perras, F. A.; Slowing, I. I.; Sadow, A. D.; Pruski, M. Dynamic Nuclear Polarization Solid-State NMR in Heterogeneous Catalysis Research. *ACS Catal.* **2015**, *5* (12), 7055-7062.

- 20. Coperet, C.; Liao, W. C.; Gordon, C. P.; Ong, T. C. Active Sites in Supported Single-Site Catalysts: An NMR Perspective. *J. Am. Chem. Soc.* **2017**, *139* (31), 10588-10596.
- 21. Vancompernolle, T.; Trivelli, X.; Delevoye, L.; Pourpoint, F.; Gauvin, R. M. On the use of Solid-State ⁴⁵Sc NMR for Structural Investigations of Molecular and Silica-Supported Scandium Amide Catalysts. *Dalton Trans.* **2017**, *46* (39), 13176-13179.
- 22. Grekov, D.; Vancompernolle, T.; Taoufik, M.; Delevoye, L.; Gauvin, R. M. Solid-State NMR of Quadrupolar Nuclei for Investigations into Supported Organometallic Catalysts: Scope and Frontiers. *Chem. Soc. Rev.* **2018**, *47* (8), 2572-2590.
- 23. Culver, D. B.; Venkatesh, A.; Huynh, H.; Rossini, A. J.; Conley, M. P. Al(OR^F)₃ (R^F = C(CF₃)₃) Activated Silica: A Well-Defined Weakly Coordinating Surface Anion. *Chem. Sci.* **2020**, *11* (6), 1510-1517.
- 24. Berruyer, P.; Lelli, M.; Conley, M. P.; Silverio, D. L.; Widdifield, C. M.; Siddiqi, G.; Gajan, D.; Lesage, A.; Coperet, C.; Emsley, L. Three-Dimensional Structure Determination of Surface Sites. *J. Am. Chem. Soc.* **2017**, *139* (2), 849-855.
- 25. Perras, F. A.; Paterson, A. L.; Syed, Z. H.; Kropf, A. J.; Kaphan, D. M.; Delferro, M.; Pruski, M. Revealing the Configuration and Conformation of Surface Organometallic Catalysts with DNP-Enhanced NMR. *J. Phys. Chem. C* **2021**, *125* (24), 13433-13442.
- 26. Zilm, K. W.; Conlin, R. T.; Grant, D. M.; Michl, J. Low-Temperature Natural-Abundance Carbon-13 NMR Spectroscopy of Matrix-Isolated Species Anisotropy of Shielding Tensor in Ethylene. *J. Am. Chem. Soc.* **1978**, *100* (25), 8038-8039.
- 27. Widdifield, C. M.; Schurko, R. W. Understanding Chemical Shielding Tensors Using Group Theory, MO Analysis, and Modern Density-Functional Theory. *Concepts Magn. Reson. Part A* **2009**, *34a* (2), 91-123.
- 28. Facelli, J. C. Chemical Shift Tensors: Theory and Application to Molecular Structural Problems. *Prog. Nucl. Magn. Reson. Spectrosc.* **2011,** *58* (3-4), 176-201.
- 29. Gordon, C. P.; Raynaud, C.; Andersen, R. A.; Coperet, C.; Eisenstein, O. Carbon-13 NMR Chemical Shift: A Descriptor for Electronic Structure and Reactivity of Organometallic Compounds. *Acc. Chem. Res.* **2019**, *52* (8), 2278-2289.
- 30. Halbert, S.; Coperet, C.; Raynaud, C.; Eisenstein, O. Elucidating the Link between NMR Chemical Shifts and Electronic Structure in d(0) Olefin Metathesis Catalysts. *J. Am. Chem. Soc.* **2016**, *138* (7), 2261-2272.
- Lummiss, J. A. M.; Perras, F. A.; McDonald, R.; Bryce, D. L.; Fogg, D. E. Sterically Driven Olefin Metathesis: The Impact of Alkylidene Substitution on Catalyst Activity. *Organometallics* **2016**, *35* (5), 691-698.
- 32. Yamamoto, K.; Gordon, C. P.; Liao, W. C.; Coperet, C.; Raynaud, C.; Eisenstein, O. Orbital Analysis of Carbon-13 Chemical Shift Tensors Reveals Patterns to Distinguish Fischer and Schrock Carbenes. *Angew. Chem. Int. Ed.* **2017**, *56* (34), 10127-10131.
- 33. Culver, D. B.; Huynh, W.; Tafazolian, H.; Ong, T. C.; Conley, M. P. The beta-Agostic Structure in (C₅Me₅)₂Sc(CH₂CH₃): Solid-State NMR Studies of (C₅Me₅)₂Sc-R (R=Me, Ph, Et). *Angew. Chem. Int. Ed.* **2018**, *57* (30), 9520-9523.
- 34. Hillenbrand, J.; Leutzsch, M.; Gordon, C. P.; Coperet, C.; Furstner, A. ¹⁸³W NMR Spectroscopy Guides the Search for Tungsten Alkylidyne Catalysts for Alkyne Metathesis. *Angew. Chem. Int. Ed.* **2020,** *59* (48), 21758-21768.
- 35. Pietrasiak, E.; Gordon, C. P.; Coperet, C.; Togni, A. Understanding ¹²⁵Te NMR chemical shifts in Disymmetric Organo-Telluride Compounds from Natural Chemical Shift Analysis. *Phys. Chem. Chem. Phys.* **2020**, *22* (4), 2319-2326.
- 36. Arduengo, A. J.; Dixon, D. A.; Kumashiro, K. K.; Lee, C.; Power, W. P.; Zilm, K. W. Chemical Shielding Tensor of a Carbene. *J. Am. Chem. Soc.* **1994**, *116* (14), 6361-6367.
- 37. Vummaleti, S. V. C.; Nelson, D. J.; Poater, A.; Gomez-Suarez, A.; Cordes, D. B.; Slawin, A. M. Z.; Nolan, S. P.; Cavallo, L. What can NMR Spectroscopy of Selenoureas and Phosphinidenes Teach us About the Pi-Accepting Abilities of N-heterocyclic Carbenes? *Chem. Sci.* **2015**, *6* (3), 1895-1904.

- 38. Engl, P. S.; Santiago, C. B.; Gordon, C. P.; Liao, W. C.; Fedorov, A.; Coperet, C.; Sigman, M. S.; Togni, A. Exploiting and Understanding the Selectivity of Ru-N-Heterocyclic Carbene Metathesis Catalysts for the Ethenolysis of Cyclic Olefins to alpha,omega-Dienes. *J. Am. Chem. Soc.* **2017**, *139* (37), 13117-13125.
- 39. Taoufik, M.; Szeto, K. C.; Merle, N.; Del Rosal, I.; Maron, L.; Trebosc, J.; Tricot, G.; Gauvin, R. M.; Delevoye, L. Heteronuclear NMR Spectroscopy as a Surface-Selective Technique: A Unique Look at the Hydroxyl Groups of gamma-Alumina. *Chem. Eur. J.* **2014**, *20* (14), 4038-4046.
- 40. Mance, D.; Comas-Vives, A.; Coperet, C. Proton-Detected Multidimensional Solid-State NMR Enables Precise Characterization of Vanadium Surface Species at Natural Abundance. *J. Phys. Chem. Lett.* **2019**, *10* (24), 7898-7904.
- 41. Love, A. M.; Cendejas, M. C.; Hanrahan, M. P.; Carnahan, S. L.; Uchupalanun, P.; Rossini, A. J.; Hermans, I. Understanding the Synthesis of Supported Vanadium Oxide Catalysts Using Chemical Grafting. *Chem. Eur. J.* **2020**, *26* (5), 1052-1063.
- 42. Corma, A.; Nemeth, L. T.; Renz, M.; Valencia, S. Sn-zeolite Beta as a Heterogeneous Chemoselective Catalyst for Baeyer-Villiger Oxidations. *Nature* **2001**, *412* (6845), 423-5.
- 43. Merle, N.; Trebosc, J.; Baudouin, A.; Rosal, I. D.; Maron, L.; Szeto, K.; Genelot, M.; Mortreux, A.; Taoufik, M.; Delevoye, L.; Gauvin, R. M. ¹⁷O NMR gives Unprecedented Insights into the Structure of Supported Catalysts and their Interaction with the Silica Carrier. *J. Am. Chem. Soc.* **2012**, *134* (22), 9263-75.
- 44. Gunther, W. R.; Michaelis, V. K.; Caporini, M. A.; Griffin, R. G.; Roman-Leshkov, Y. Dynamic Nuclear Polarization NMR Enables the Analysis of Sn-Beta Zeolite Prepared with Natural Abundance ¹¹⁹Sn Precursors. *J. Am. Chem. Soc.* **2014**, *136* (17), 6219-22.
- 45. Delley, M. F.; Lapadula, G.; Nunez-Zarur, F.; Comas-Vives, A.; Kalendra, V.; Jeschke, G.; Baabe, D.; Walter, M. D.; Rossini, A. J.; Lesage, A.; Emsley, L.; Maury, O.; Coperet, C. Local Structures and Heterogeneity of Silica-Supported M(III) Sites Evidenced by EPR, IR, NMR, and Luminescence Spectroscopies. *J. Am. Chem. Soc.* **2017**, *139* (26), 8855-8867.
- 46. Camacho-Bunquin, J.; Ferrandon, M.; Sohn, H.; Yang, D. L.; Liu, C.; Ignacio-de Leon, P. A.; Perras, F. A.; Pruski, M.; Stair, P. C.; Delferro, M. Chemoselective Hydrogenation with Supported Organoplatinum(IV) Catalyst on Zn(II)-Modified Silica. *J. Am. Chem. Soc.* **2018**, *140* (11), 3940-3951.
- 47. Perras, F. A.; Boteju, K. C.; Slowing, II; Sadow, A. D.; Pruski, M. Direct ¹⁷O Dynamic Nuclear Polarization of Single-Site Heterogeneous Catalysts. *Chem. Commun.* **2018**, *54* (28), 3472-3475.
- 48. Nagashima, H.; Trebosc, J.; Kon, Y.; Sato, K.; Lafon, O.; Amoureux, J. P. Observation of Lowgamma Quadrupolar Nuclei by Surface-Enhanced NMR Spectroscopy. *J. Am. Chem. Soc.* **2020**, *142* (24), 10659-10672.
- 49. Ishizaka, Y.; Arai, N.; Matsumoto, K.; Nagashima, H.; Takeuchi, K.; Fukaya, N.; Yasuda, H.; Sato, K.; Choi, J. C. Bidentate Disilicate Framework for Bis-Grafted Surface Species. *Chem. Eur. J.* **2021**, *27* (47), 12069-12077.
- 50. Fu, Q.; Saltsburg, H.; Flytzani-Stephanopoulos, M. Active Nonmetallic Au and Pt Species on Ceria-based Water-Gas Shift Catalysts. *Science* **2003**, *301* (5635), 935-938.
- Vajda, S.; Pellin, M. J.; Greeley, J. P.; Marshall, C. L.; Curtiss, L. A.; Ballentine, G. A.; Elam, J. W.; Catillon-Mucherie, S.; Redfern, P. C.; Mehmood, F.; Zapol, P. Subnanometre Platinum Clusters as Highly Active and Selective Catalysts for the Oxidative Dehydrogenation of Propane. *Nat. Mater.* **2009**, *8* (3), 213-216.
- 52. Qiao, B. T.; Wang, A. Q.; Yang, X. F.; Allard, L. F.; Jiang, Z.; Cui, Y. T.; Liu, J. Y.; Li, J.; Zhang, T. Single-atom catalysis of CO oxidation using Pt-1/FeOx. *Nat. Chem.* **2011**, *3* (8), 634-641.
- 53. MacGregor, A. W.; O'Dell, L. A.; Schurko, R. W. New Methods for the Acquisition of Ultra-Wideline Solid-State NMR Spectra of Spin-1/2 Nuclides. *J. Magn. Reson.* **2011**, *208* (1), 103-113.
- 54. Schurko, R. W. Ultra-Wideline Solid-State NMR Spectroscopy. *Acc. Chem. Res.* **2013**, *46* (9), 1985-1995.

- 55. Lucier, B. E. G.; Johnston, K. E.; Xu, W. Q.; Hanson, J. C.; Senanayake, S. D.; Yao, S. Y.; Bourassa, M. W.; Srebro, M.; Autschbach, J.; Schurko, R. W. Unravelling the Structure of Magnus' Pink Salt. *J. Am. Chem. Soc.* **2014**, *136* (4), 1333-1351.
- 56. Austin, E. J. W.; Barrie, P. J.; Clark, R. J. H. Solid-State ¹⁹⁵Pt NMR-Studies of the Complexes Pt(En)Cl_x (En = 1,2-Diaminoethane x = 2,3 or 4). *J. Chem. Soc., Chem. Commun.* **1993**, (18), 1404-1405.
- 57. Sparks, S. W.; Ellis, P. D. ¹⁹⁵Pt Shielding Tensors in Potassium Hexachloroplatinate(IV) and Potassium Tetrachloroplatinate(II). *J. Am. Chem. Soc.* **1986,** *108* (12), 3215-3218.
- 58. Sterzel, M.; Autschbach, J. Toward an Accurate Determination of ¹⁹⁵Pt Chemical Shifts by Density Functional Computations: The Importance of Unspecific Solvent Effects and the Dependence of Pt Magnetic Shielding Constants on Structural Parameters. *Inorg. Chem.* **2006**, *45* (8), 3316-3324.
- 59. Autschbach, J.; Zheng, S. H. Analyzing Pt Chemical Shifts Calculated from Relativistic Density Functional Theory Using Localized Orbitals: The Role of Pt 5d Lone Pairs. *Magn. Reson. Chem.* **2008**, *46*, S45-S55.
- 60. Lucier, B. E. G.; Reidel, A. R.; Schurko, R. W. Multinuclear Solid-State NMR of Square-Planar Platinum Complexes Cisplatin and Related Systems. *Can. J. Chem.* **2011**, *89* (7), 919-937.
- 61. Siegel, R.; Nakashima, T. T.; Wasylishen, R. E. Application of Multiple-Pulse Experiments to Characterize Broad NMR Chemical-Shift Powder Patterns from Spin-1/2 Nuclei in the Solid State. *J. Phys. Chem. B* **2004**, *108* (7), 2218-2226.
- 62. Harris, K. J.; Lupulescu, A.; Lucier, B. E. G.; Frydman, L.; Schurko, R. W. Broadband Adiabatic Inversion Pulses for Cross Polarization in Wideline Solid-State NMR Spectroscopy. *J. Magn. Reson.* **2012,** *224*, 38-47.
- 63. Altenhof, A. R.; Jaroszewicz, M. J.; Lindquist, A. W.; Foster, L. D. D.; Veinberg, S. L.; Schurko, R. W. Practical Aspects of Recording Ultra-Wideline NMR Patterns under Magic-Angle Spinning Conditions. *J. Phys. Chem. C* **2020**, *124* (27), 14730-14744.
- 64. Kobayashi, T.; Perras, F. A.; Goh, T. W.; Metz, T. L.; Huang, W. Y.; Pruski, M. DNP-Enhanced Ultrawideline Solid-State NMR Spectroscopy: Studies of Platinum in Metal-Organic Frameworks. *J. Phys. Chem. Lett.* **2016**, *7* (13), 2322-2327.
- 65. Kobayashi, T.; Perras, F. A.; Murphy, A.; Yao, Y.; Catalano, J.; Centeno, S. A.; Dybowski, C.; Zumbulyadis, N.; Pruski, M. DNP-Enhanced Ultrawideline Pb-207 Solid-State NMR Spectroscopy: an Application to Cultural Heritage Science. *Dalton Trans.* **2017**, *46* (11), 3535-3540.
- 66. Venkatesh, A.; Lund, A.; Rochlitz, L.; Jabbour, R.; Gordon, C. P.; Menzildjian, G.; Viger-Gravel, J.; Berruyer, P.; Gajan, D.; Copéret, C.; Lesage, A.; Rossini, A. J. The Structure of Molecular and Surface Platinum Sites Determined by DNP-SENS and Fast MAS ¹⁹⁵Pt Solid-State NMR Spectroscopy. *J. Am. Chem. Soc.* **2020**, *142* (44), 18936-18945.
- 67. Ishii, Y.; Yesinowski, J. P.; Tycko, R. Sensitivity Enhancement in Solid-State ¹³C NMR of Synthetic Polymers and Biopolymers by ¹H NMR Detection with High-Speed Magic Angle Spinning. *J. Am. Chem. Soc.* **2001**, *123* (12), 2921-2922.
- 68. Reif, B.; Griffin, R. G. ¹H Detected ¹H-¹⁵N Correlation Spectroscopy in Rotating Solids. *J. Magn. Reson.* **2003**, *160* (1), 78-83.
- 69. Poppler, A. C.; Demers, J. P.; Malon, M.; Singh, A. P.; Roesky, H. W.; Nishiyama, Y.; Lange, A. Ultrafast Magic-Angle Spinning: Benefits for the Acquisition of Ultrawide-Line NMR Spectra of Heavy Spin-1/2 Nuclei. *ChemPhysChem* **2016**, *17* (6), 812-816.
- 70. Kobayashi, T.; Nishiyama, Y.; Pruski, M. Heteronuclear Correlation Solid-state NMR Spectroscopy with Indirect Detection under Fast Magic-Angle Spinning. In *Modern Methods in Solid-state NMR: A Practitioner's Guide*, Hodgkinson, P., Ed. The Royal Society of Chemistry: **2018**; pp 1-38.
- 71. Rossini, A. J.; Hanrahan, M. P.; Thuo, M. Rapid Acquisition of Wideline MAS Solid-State NMR Spectra with Fast MAS, Proton Detection, and Dipolar HMQC Pulse Sequences. *Phys. Chem. Chem. Phys.* **2016**, *18* (36), 25284-25295.
- 72. Perras, F. A.; Venkatesh, A.; Hanrahan, M. P.; Goh, T. W.; Huang, W.; Rossini, A. J.; Pruski, M. Indirect Detection of Infinite-Speed MAS Solid-State NMR Spectra. *J. Magn. Reson.* **2017**, *276*, 95-102.

- 73. Li, Y. X.; Trebosc, J.; Hu, B. W.; Shen, M.; Amoureux, J. P.; Lafon, O. Indirect detection of Broad Spectra in Solid-State NMR Using Interleaved DANTE Trains. *J. Magn. Reson.* **2018**, *294*, 101-114.
- 74. Venkatesh, A.; Perras, F. A.; Rossini, A. J. Proton-Detected Solid-State NMR Spectroscopy of Spin-1/2 Nuclei with Large Chemical Shift Anisotropy. *J. Magn. Reson.* **2021**, *327*, 106983.
- 75. Paluch, P.; Rankin, A. G. M.; Trebosc, J.; Lafon, O.; Amoureux, J. P. Analysis of HMQC Experiments Applied to a Spin 1/2 Nucleus Subject to Very Large CSA. *Solid State Nucl. Magn. Reson.* **2019**, *100*, 11-25.
- 76. Grey, C. P.; Vega, A. J. Determination of the Quadrupole Coupling-Constant of the Invisible Aluminum Spins in Zeolite HY with ¹H/²⁷Al TRAPDOR NMR. *J. Am. Chem. Soc.* **1995**, *117* (31), 8232-8242.
- 77. Grey, C. P.; Veeman, W. S. The Detection of Weak Heteronuclear Coupling between Spin-1 and Spin-1/2 Nuclei in MAS NMR; ¹⁴N/¹³C/¹H Triple Resonance Experiments. *Chem. Phys. Lett.* **1992**, *192* (4), 379-385.
- 78. Kalwei, M.; Koller, H. Quantitative Comparison of REAPDOR and TRAPDOR Experiments by Numerical Simulations and Determination of H-Al Distances in Zeolites. *Solid State Nucl. Magn. Reson.* **2002**, *21* (3-4), 145-157.
- 79. Gan, Z. H. Measuring Nitrogen Quadrupolar Coupling with ¹³C Detected Wide-line ¹⁴N NMR under Magic-Angle Spinning. *Chem. Commun.* **2008**, (7), 868-870.
- 80. Duong, N. T.; Nishiyama, Y. Detection of Remote Proton-Nitrogen Correlations by ¹H-Detected ¹⁴N Overtone Solid-State NMR at Fast MAS. *Phys. Chem. Chem. Phys.* **2022**, *24* (18), 10717-10726.
- 81. Jaroszewicz, M. J.; Altenhof, A. R.; Schurko, R. W.; Frydman, L. Sensitivity Enhancement by Progressive Saturation of the Proton Reservoir: A Solid-State NMR Analogue of Chemical Exchange Saturation Transfer. *J. Am. Chem. Soc.* **2021**, *143* (47), 19778-19784.
- 82. Bak, M.; Rasmussen, J. T.; Nielsen, N. C. SIMPSON: A General Simulation Program for Solid-State NMR Spectroscopy. *J. Magn. Reson.* **2000**, *147* (2), 296-330.
- 83. Tosner, Z.; Vosegaard, T.; Kehlet, C.; Khaneja, N.; Glaser, S. J.; Nielsen, N. C. Optimal Control in NMR Spectroscopy: Numerical Implementation in SIMPSON. *J. Magn. Reson.* **2009**, *197* (2), 120-134.
- 84. Tosner, Z.; Andersen, R.; Stevenss, B.; Eden, M.; Nielsen, N. C.; Vosegaard, T. Computer-Intensive Simulation of Solid-State NMR Experiments using SIMPSON. *J. Magn. Reson.* **2014**, *246*, 79-93.
- 85. Brinkmann, A.; Kentgens, A. P. M. Proton-Selective ¹⁷O-¹H Distance Measurements in Fast Magic Angle Spinning Solid-State NMR Spectroscopy for the Determination of Hydrogen Bond Lengths. *J. Am. Chem. Soc.* **2006**, *128* (46), 14758-14759.
- 86. Venkatesh, A.; Luan, X.; Perras, F. A.; Hung, I.; Huang, W.; Rossini, A. J. t₁-Noise Eliminated Dipolar Heteronuclear Multiple-Quantum Coherence Solid-State NMR Spectroscopy. *Phys. Chem. Chem. Phys.* **2020**, *22*, 20815-20828.
- 87. Parella, T. Towards Perfect NMR: Spin-Echo versus Perfect-Echo Building Blocks. *Magn. Reson. Chem.* **2019**, *57* (1), 13-29.
- 88. Duong, N. T.; Rossi, F.; Makrinich, M.; Goldbourt, A.; Chierotti, M. R.; Gobetto, R.; Nishiyama, Y. Accurate ¹H-¹⁴N Distance Measurements by Phase-Modulated RESPDOR at Ultra-Fast MAS. *J. Magn. Reson.* **2019**, *308*, 106559.
- 89. Perras, F. A.; Pruski, M. Reducing *t*₁ Noise through Rapid Scanning. *J. Magn. Reson.* **2019**, *298*, 31-34.
- 90. Atterberry, B. A.; Carnahan, S. L.; Chen, Y.; Venkatesh, A.; Rossini, A. J. Double Echo Symmetry-Based REDOR and RESPDOR Pulse Sequences for Proton Detected Measurements of Heteronuclear Dipolar Coupling Constants. *J. Magn. Reson.* **2022**, *336*, 107147.
- 91. Ha, K. Crystal structure of bis(pentane-2,4-dionato-kappa O-2,O ')platinum(II), Pt(C₅H₇O₂)₂. *Z. Kristallogr. NCS* **2011**, *226* (3), 329-330.

- 92. Dechter, J. J.; Kowalewski, J. ¹⁹⁵Pt Spin-Lattice Relaxation and Shielding Anisotropy for Pt(Acac)₂. *J. Magn. Reson.* **1984**, *59* (1), 146-149.
- 93. Ruddy, D. A.; Jarupatrakorn, J.; Rioux, R. M.; Miller, J. T.; McMurdo, M. J.; Mcbee, J. L.; Tupper, K. A.; Tilley, T. D. Site-Isolated Pt-SBA15 Materials from Tris(tert-butoxy)siloxy Complexes of Pt(II) and Pt(IV). *Chem. Mater.* **2008**, *20* (20), 6517-6527.
- 94. Goikhman, R.; Aizenberg, M.; Shimon, L. J. W.; Milstein, D. Transition Metal-Catalyzed Silanone Generation. *J. Am. Chem. Soc.* **1996**, *118* (44), 10894-10895.
- 95. Autschbach, J. The Role of the Exchange-Correlation Response Kernel and Scaling Corrections in Relativistic Density Functional Nuclear Magnetic Shielding Calculations with the Zeroth-Order Regular Approximation. *Mol Phys* **2013**, *111* (16-17), 2544-2554.
- 96. vanLenthe, E.; Snijders, J. G.; Baerends, E. J. The Zero-Order Regular Approximation for Relativistic Effects: The Effect of Spin-Orbit Coupling in Closed Shell Molecules. *J. Chem. Phys.* **1996**, *105* (15), 6505-6516.
- 97. Davis, J. C.; Buhl, M.; Koch, K. R. On the Origin of ^{35/37}Cl Isotope Effects on ¹⁹⁵Pt NMR Chemical Shifts. A Density Functional Study. *J. Chem. Theory Comput.* **2012**, *8* (4), 1344-1350.
- 98. Bryce, D. L. NMR Crystallography: Structure and Properties of Materials from Solid-State Nuclear Magnetic Resonance Observables. *Iucrj* **2017**, *4*, 350-359.
- 99. Hodgkinson, P. NMR Crystallography of Molecular Organics. *Prog. Nucl. Magn. Reson. Spectrosc.* **2020**, *118-119*, 10-53.
- 100. Gilbert, T. M.; Ziegler, T. Prediction of ¹⁹⁵Pt NMR Chemical Shifts by Density Functional Theory Computations: The Importance of Magnetic Coupling and Relativistic Effects in Explaining Trends. *J. Phys. Chem. A* **1999**, *103* (37), 7535-7543.
- 101. Frisch, M. J.; Trucks, G. W.; Schlegel, H. B.; Scuseria, G. E.; Robb, M. A.; Cheeseman, J. R.; Scalmani, G.; Barone, V.; Mennucci, B.; Petersson, G. A.; Nakatsuji, H.; Caricato, M.; Li, X.; Hratchian, H. P.; Izmaylov, A. F.; Bloino, J.; Zheng, G.; Sonnenberg, J. L.; Hada, M.; Ehara, M.; Toyota, K.; Fukuda, R.; Hasegawa, J.; Ishida, M.; Nakajima, T.; Honda, Y.; Kitao, O.; Nakai, H.; Vreven, T.; Montgomery, J. A.; Peralta, J. J. E.; Ogliaro, F.; Bearpark, M.; Heyd, J. J.; Brothers, E.; Kudin, K. N.; Staroverov, V. N.; Kobayashi, R.; Normand, J.; Raghavachari, K.; Rendell, A.; Burant, J. C.; Iyengar, S. S.; Tomasi, J.; Cossi, M.; Rega, N.; Millam, J. M.; Klene, M.; Knox, J. E.; Cross, J. B.; Bakken, V.; Adamo, C.; Jaramillo, J.; Gomperts, R.; Stratmann, R. E.; Yazyev, O.; Austin, A. J.; Cammi, R.; Pomelli, C.; Ochterski, J. W.; Martin, R. L.; Morokuma, K.; Zakrzewski, V. G.; Voth, G. A.; Salvador, P.; Dannenberg, J. J.; Dapprich, S.; Daniels, A. D.; Farkas, Ö.; Foresman, J. B.; Ortiz, J. V.; Cioslowski, J.; Fox, D. J. *Gaussian 09 Version D.01*, Gaussian Inc.: Wallingford, CT, 2009.
- 102. te Velde, G.; Bickelhaupt, F. M.; Baerends, E. J.; Guerra, C. F.; Van Gisbergen, S. J. A.; Snijders, J. G.; Ziegler, T. Chemistry with ADF. *J. Comput. Chem.* **2001**, *22* (9), 931-967.
- 103. Sandoval, J. J.; Palma, P.; Alvarez, E.; Campora, J.; Rodriguez-Delgado, A. Mechanism of Alkyl Migration in Diorganomagnesium 2,6-Bis(imino)pyridine Complexes: Formation of Grignard-Type Complexes with Square-Planar Mg(II) Centers. *Organometallics* **2016**, *35* (18), 3197-3204.
- 104. Su, K.; Tilley, T. D.; Sailor, M. J. Molecular and Polymer Precursor Routes to Manganese-Doped Zinc Orthosilicate Phosphors. *J. Am. Chem. Soc.* **1996**, *118* (14), 3459-3468.
- 105. Smith, D. C.; Haar, C. M.; Stevens, E. D.; Nolan, S. P.; Marshall, W. J.; Moloy, K. G. Synthetic, Structural, and Solution Calorimetric Studies of Pt(CH₃)₂(PP) Complexes. *Organometallics* **2000**, *19* (7), 1427-1433.
- 106. Searles, K.; Siddiqi, G.; Safonova, O. V.; Coperet, C. Silica-Supported Isolated Gallium Sites as Highly Active, Selective and Stable Propane Dehydrogenation Catalysts. *Chem. Sci.* **2017**, *8* (4), 2661-2666.
- 107. Yanai, T.; Tew, D. P.; Handy, N. C. A New Hybrid Exchange-Correlation Functional using the Coulomb-Attenuating Method (CAM-B3LYP). *Chem. Phys. Lett.* **2004**, *393* (1-3), 51-57.
- 108. Rassolov, V. A.; Pople, J. A.; Ratner, M. A.; Windus, T. L. 6-31G* Basis Set for Atoms K through Zn. *J. Chem. Phys.* **1998**, *109* (4), 1223-1229.

- 109. Roy, L. E.; Hay, P. J.; Martin, R. L. Revised Basis Sets for the LANL Effective Core Potentials. *J. Chem. Theory Comput.* **2008**, *4* (7), 1029-1031.
- 110. vanLenthe, E.; vanLeeuwen, R.; Baerends, E. J.; Snijders, J. G. Relativistic Regular Two-Component Hamiltonians. *Int. J. Quantum Chem.* **1996**, *57* (3), 281-293.
- 111. Zurek, E.; Pickard, C. J.; Autschbach, J. Density Functional Study of the ¹³C NMR Chemical Shifts in Single-Walled Carbon Nanotubes with Stone-Wales Defects. *J. Phys. Chem. C* **2008**, *112* (31), 11744-11750.
- 112. Clark, S. J.; Segall, M. D.; Pickard, C. J.; Hasnip, P. J.; Probert, M. J.; Refson, K.; Payne, M. C. First Principles Methods using CASTEP. *Z. Kristallogr.* **2005**, *220* (5-6), 567-570.
- 113. Perdew, J. P.; Burke, K.; Ernzerhof, M. Generalized Gradient Approximation Made Simple. *Phys. Rev. Lett.* **1996,** 77 (18), 3865-3868.
- 114. Tkatchenko, A.; Scheffler, M. Accurate Molecular Van Der Waals Interactions from Ground-State Electron Density and Free-Atom Reference Data. *Phys. Rev. Lett.* **2009**, *102* (7), 073005.
- 115. van Meerten, S. G. J.; Franssen, W. M. J.; Kentgens, A. P. M. ssNake: A Cross-Platform Open-Source NMR Data Processing and Fitting Application. *J. Magn. Reson.* **2019**, *301*, 56-66.
- 116. Oas, T. G.; Griffin, R. G.; Levitt, M. H. Rotary Resonance Recoupling of Dipolar Interactions in Solid-State Nuclear Magnetic-Resonance Spectroscopy. *J. Chem. Phys.* **1988**, *89* (2), 692-695.
- 117. Venkatesh, A.; Hung, I.; Boteju, K. C.; Sadow, A. D.; Gor'kov, P. L.; Gan, Z.; Rossini, A. J. Suppressing ¹H Spin Diffusion in Fast MAS Proton Detected Heteronuclear Correlation Solid-State NMR Experiments. *Solid State Nucl. Magn. Reson.* **2020**, *105*, 101636.
- 118. Herzfeld, J.; Berger, A. E. Sideband Intensities in NMR Spectra of Samples Spinning at the Magic Angle. *J. Chem. Phys.* **1980**, *73* (12), 6021-6030.
- 119. Eichele, K. HBA 1.7.5, Universität Tübingen, 2015.
- 120. Fung, B. M.; Khitrin, A. K.; Ermolaev, K. An Improved Broadband Decoupling Sequence for Liquid Crystals and Solids. *J. Magn. Reson.* **2000,** *142*, 97-101.